Remote Sensing of Environment 113 (2009) 571–587

Contents lists available at ScienceDirect

Remote Sensing of Environment

journal homepage: www.elsevier.com/locate/rse

Spectral optimization for constituent retrieval in Case 2 waters I: Implementation and performance

Christopher P. Kuchinke [a], Howard R. Gordon [a,*], Bryan A. Franz [b]

[a] Department of Physics, University of Miami, PO Box 248046, Coral Gables, FL 33124, USA
[b] SAIC, Ocean Biology Processing Group, NASA/GSFC, Greenbelt, MD 20771, USA

ARTICLE INFO

Article history:
Received 2 June 2006
Received in revised form 31 October 2008
Accepted 1 November 2008

Keywords:
Remote Sensing
Ocean color
Case 2 waters
Atmospheric correction
Aerosol absorption
Chlorophyll a
Colored Dissolved Material
Backscattering
Bio-optical coefficients

ABSTRACT

We describe in detail the implementation of the spectral optimization algorithm (SOA) for Case 2 waters for processing of ocean color data. This algorithm uses aerosol models and a bio-optical reflectance model to provide the top-of atmosphere (TOA) reflectance. The parameters of both models are then determined by fitting the modeled TOA reflectance to that observed from space, using non-linear optimization. The algorithm will be incorporated into the SeaDAS software package as an optional processing switch of the Multi-Sensor Level-1 to Level-2 code. To provide potential users with an understanding of the accuracy and limitations of the algorithm, we generated a synthetic data set and tested the performance of the SOA with both correct and incorrect bio-optical model parameters. Application of the SOA to actual SeaWiFS data in the Lower Chesapeake Bay (for which surface measurements were available) showed that 20% errors in the bio-optical model parameters still enabled retrieval of chlorophyll *a* and the total absorption coefficient of dissolved plus particulate detrital material at 443 nm with an error of less than 30% and 20%, respectively. In a companion paper we present a validation study of the application of the algorithm in the Chesapeake Bay.

1. Introduction

Since the Coastal Zone Color Scanner (CZCS) proof-of-concept ocean color mission (Gordon et al., 1980; Hovis et al., 1980; Gordon & Morel, 1983), space borne monitoring of the concentration of phytoplankton pigments, particularly chlorophyll *a*, has become well established. Two sensors, the Sea-viewing Wide Field of View Sensor (SeaWiFS) and Moderate Resolution Imaging Spectroradiometer (MODIS) were launched in 1997 and 1999, respectively, and a second MODIS in 2002. They represent considerable improvements in radiometric sensitivity over CZCS (Hooker et al., 1992; Salomonson et al., 1989). This necessitated the need for more sophisticated algorithms both for atmospheric correction, to retrieve the water leaving reflectance ρ_w from the total reflectance ρ_t measured at the top of the atmosphere, and for bio-optical retrieval, relating ρ_w to the chlorophyll concentration. Here, we focus on SeaWiFS, which has 6 spectral bands in the visible (VIS, bands 1–6: 412, 443, 490, 510, 555, and 670 nm) and 2 bands in the near infrared (NIR, bands 7 and 8: 765 and 865 nm); however, the results should be applicable to any sensor with a similar band set.

The SeaWiFS data analysis system (SeaDAS: oceancolor.gsfc.nasa.gov/seadas/) provides the framework for both atmospheric correction and bio-optical retrievals from ρ_t using both SeaWiFS and MODIS. At present, only one standard atmospheric correction is available (Gordon & Wang, 1994; Gordon, 1997). The algorithm compares the spectral variation of the aerosol reflectance ρ_A in the near infrared (NIR) with that of several candidate aerosol physical–chemical bimodal models (Shettle & Fenn, 1979). The most appropriate models are then used in estimating the aerosol contribution in the visible spectrum. This technique appears to work well if the aerosol is non-absorbing (Bailey & Werdell, 2006), however the NIR measurements alone make it impossible to infer information about aerosol absorption (Gordon, 1997). For this task it becomes necessary to include information at visible wavelengths in the correction process. The difficulty then becomes retrieval of the water leaving reflectance ρ_w at the same wavelengths, whose estimate is dependent on the absorption and scattering properties of the unknown water constituents. Essentially the task requires a coupled model for simultaneous characterization of ρ_A and ρ_w. Two examples of such a method are the spectral matching algorithm (Gordon et al., 1997) and the spectral optimization algorithm SOA (Chomko & Gordon, 1998; Chomko & Gordon, 2001). The latter model will be the focus of discussion in this study. It assumes a simple one-parameter model for the aerosol size distribution. A set of refractive indices that represents a range of absorption properties is then used in conjunction with Mie theory to yield the aerosol optical properties. These aerosol models are then combined with a bio-optical model to estimate the aerosol and water properties through non-linear optimization.

The two mentioned SOA studies use the semi-analytic bio-optical model of Gordon et al. (1988) for retrieval of chlorophyll information

PII of original article: S0034-4257(08)00329-5.
* Corresponding author.
E-mail address: gordon@physics.miami.edu (H.R. Gordon).

0034-4257/$ – see front matter © 2008 Elsevier Inc. All rights reserved.
doi:10.1016/j.rse.2008.11.001

assisted by a marine particulate scattering factor b_0. A more recent bio-optical model by Garver and Siegel (1997), denoted GSM after its optimized tuning by Maritorena et al. (2002), retrieves chlorophyll information, particulate backscatter b_{bp} and the absorption by colored detrital material (CDM, the sum of dissolved organic matter and detrital particles). The SOA coupled with a Case 1 version of GSM was first developed by Chomko et al. (2003). It performed well retrieving the chlorophyll *a* concentration and the absorption of detrital material in Case 1 waters when the aerosol was non- or weakly-absorbing; however, in this situation it performed no better than the Gordon and Wang atmospheric correction algorithm combined with GSM. The attraction of the SOA is its potential to provide adequate retrievals when the aerosol is more strongly absorbing.

This study presents a new version of the SOA to be incorporated into the SeaDAS software package, as an optional processing switch of the Multi-Sensor Level-1 to Level-2 code (Franz et al., 2005). It contains an updated non-linear spectral optimization and is modified to operate in Case 2 waters as defined in Gordon and Morel (1983). From an ocean color perspective, Case 2 waters are challenging for several reasons. First, they often contain concentrations of particulates (organic and inorganic) that are sufficiently high to produce significant water reflectance in the NIR. Thus, the basic assumption in the Gordon and Wang (1994) atmospheric correction algorithm, i.e., that the reflectance in the NIR is negligible, is violated. Second, admitting that many Case 2 waters are in coastal areas, the aerosol over such waters is more likely to be absorbing due to the proximity to land and anthropogenic sources of pollution. The effect on the reflectance at the top of the atmosphere by the associated absorption by such aerosols in the blue must be separated from the effect of the phytoplankton pigments and the detrital material in the water. For these reasons, we concentrate here on Case 2 waters.

The SOA as presented earlier (Chomko et al., 2003) is modified to handle situations in which NIR reflectivity is non-negligible in an iterative manner. A complete summary of the model is presented here, including a detailed description of the interpolation framework used for determination of all parameters and the modifications required for Case 2 waters. The SOA is then tested using a simulated Case 2 data set to quantify its performance.

For this task two sets of GSM model parameters are examined using information from the Lower Chesapeake Bay (CBL) and the Middle Atlantic Bight (MAB). The performance of the model in each Case 2 region is determined to provide an understanding of the strengths and limitations of the algorithm.

Understanding that Case 2 waters are sufficiently diverse and complex that a "universal" set of Case 2 bio-optical model parameters simply does not exist, and site-specific, and likely time-specific, bio-optical parameters will be required, an analysis of the impact of error in the GSM model parameters (i.e., error in the assumed bio-optical model parameters) on SOA performance is also presented using synthetic data in CBL and MAB, as well as SeaWiFS data in CBL. The overall goal is to provide examples of the error that might be expected in an actual application of the algorithm, so a user might judge the likely quality of a given retrieval. In a companion paper, we provide a case study of the application and performance of the modified SOA in the Chesapeake Bay through comparisons with contemporaneous *in situ* data (Kuchinke et al., 2009).

2. Radiative properties of the model

2.1. Radiative transfer

Throughout we use the reflectance ρ in place of the radiance L. The reflectance is defined by $\rho=\pi L/F_0\cos\theta_s$, where F_0 is the extraterrestrial solar irradiance and θ_s is the solar zenith angle. After removing sun-glint contaminated pixels and correcting for whitecap reflectance using the standard SeaDAS algorithms, we obtain the total top-of-atmosphere (TOA) reflectance of the ocean-atmosphere system $\rho_t(\lambda)$ at visible and NIR wavelengths λ. This quantity includes the molecular Rayleigh scattering contribution $\rho_r(\lambda)$, the aerosol contribution in the presence of Rayleigh scattering $\rho_A(\lambda)$, and the TOA water-leaving reflectance $t_v(\lambda)t_s(\lambda)\rho_w(\lambda)$; i.e.,

$$\rho_t(\lambda)=\rho_r(\lambda)+\rho_A(\lambda)+t_v(\lambda)t_s(\lambda)\rho_w(\lambda), \tag{1}$$

where $t_s(\lambda)$ and $t_v(\lambda)$ are the atmospheric diffuse transmittances from the sun to the sea surface and sensor to the sea surface, respectively. The atmospheric contribution $\rho_r(\lambda)+\rho_A(\lambda)$ includes light scattered in the atmosphere and specularly reflected from the sea surface, as well as sunlight directly backscattered from the atmosphere alone. Since $\rho_r(\lambda)$ can be computed precisely given the surface atmospheric pressure and wind speed, it can be subtracted from $\rho_t(\lambda)$ to form

$$\begin{aligned}\rho_{Aw}(\theta_s,\theta_v,\phi,\lambda,\text{measured})\equiv&\rho_A(\theta_s,\theta_v,\phi,\lambda)\\&+t_v(\theta_s,\theta_v,\phi,\lambda)t_s(\theta_s,\theta_v,\phi,\lambda)\rho_w(\lambda)\end{aligned} \tag{2}$$

where θ_s, θ_v and ϕ represent the solar and viewing zenith angles and relative azimuth angles respectively. The final result also includes an aerosol and Rayleigh correction for oxygen absorption in SeaWiFS band 7 (Ding & Gordon, 1995).

2.2. The aerosol models

Aerosol particles are distributed according to a Junge power-law size distribution (Chomko & Gordon, 1998):

$$\begin{aligned}&\frac{dN}{dD}=0,\quad D<D_0,\\&\frac{dN}{dD}=\frac{K}{D_1^{\nu+1}},\quad D_0\le D\le D_1,\\&\frac{dN}{dD}=\frac{K}{D^{\nu+1}},\quad D_1\le D\le D_2,\\&\frac{dN}{dD}=0,\quad D>D_2,\end{aligned} \tag{3}$$

where D and dN are the particle diameter and number of particles per unit volume in the size interval $D\pm dD/2$, and D_0, D_1 and D_2 are 0.06, 0.20 and 20 μm respectively. This size distribution has been used often to represent aerosols, although many recent studies show that it is an oversimplification (see Kaufman et al., 1997 and papers therein). We use it here because with D_0, D_1, and D_2 fixed, the size distribution depends continuously on a single parameter: ν. This oversimplified parameterization is required due to the small number of spectral bands available for the optimization.

A single wavelength-independent complex index of refraction $m=m_r-im_i$ is assigned to the entire distribution to compute the radiative optical properties from Mie theory, i.e., the aerosol phase function, aerosol optical depth $\tau(\lambda)$, and aerosol single-scattering albedo $\omega_0(\lambda)$. A two-layer radiative transfer (RT) program was used to compute the reflectance for the atmosphere-sea surface system providing $\rho_r(\lambda)+\rho_A(\lambda)$, as a function of the aerosol optical depth at 865 nm, $\tau(865)$. In the case of strongly absorbing aerosols, $\rho_r(\lambda)+\rho_A(\lambda)$ depends strongly on the altitude to which the aerosol is mixed. In these computations the aerosol was uniformly mixed with air from the surface up to 2 km. The choice of mixing to 2 km was again a compromise to reduce the number of parameters to allow optimization. In the RT computations, the atmosphere was bounded by a flat Fresnel reflecting ocean that absorbed all photons penetrating the surface. Computing $\rho_t(\lambda)-\rho_r(\lambda)$ produced $\rho_A(\lambda)$ as a function of $\tau(\lambda)$, with λ centered at the respective wavelength of the SeaWiFS bands. This final result was least-squares fit to a quartic expression for $\tau(\lambda)=0$ to 1.2 over a wide range of solar and viewing geometries.

$$\begin{aligned}\rho_A(\theta_s,\theta_v,\phi,\lambda,m_r,m_i,\nu)=&\,a(\theta_s,\theta_v,\phi,\lambda,m_r,m_i,\nu)\tau(\lambda)\\&+b(\theta_s,\theta_v,\phi,\lambda,m_r,m_i,\nu)\tau^2(\lambda)\\&+c(\theta_s,\theta_v,\phi,\lambda,m_r,m_i,\nu)\tau^3(\lambda)\\&+d(\theta_s,\theta_v,\phi,\lambda,m_r,m_i,\nu)\tau^4(\lambda)\end{aligned} \tag{4}$$

where a, b, c, d are fitted constants for a given geometry. We mention in passing detail that a, b, c, d are actually computed from their Fourier transformed (in the angle ϕ) counterparts to reduce the size of the final look-up tables (LUTs). This is the same technique that is used in the LUTs stored for the standard Gordon and Wang (1994) algorithm.

The information on aerosols is stored in the form of 72 LUTs for access by the SOA. The complex index of refraction is indexed into two values of m_r (1.33, 1.5) and six values of m_i (0, 0.001, 0.002, 0.004, 0.007, 0.010). More values of m_i are used than m_r in an attempt to include as much of the variation in absorbing properties of the aerosol as possible within a limited range of models. The Junge aerosol size distribution parameter ν ranges from 2.0 to 4.5 in steps of 0.5. Each of the models in the LUTs therefore contains RT information calculated for the specific combination of m_i, m_r and ν, namely the extinction coefficient $k(\lambda)$ (for an arbitrary K), the single scattering albedo $\omega_0(\lambda)$, and the a, b, c, d (Fourier analyzed) coefficients relating $\rho_A(\lambda)$ and $\tau(\lambda)$ for a large set of viewing and solar directions. For the diffuse transmittance we use the same assumption as the standard algorithm, i.e., that the upwelling radiance beneath the water surface is uniform, such that $t_v(\theta_s,\theta_v,\phi,\lambda)\rightarrow t^*(\theta_v\lambda)$ and $t_s(\theta_s,\theta_v,\phi,\lambda)\rightarrow t^*(\theta_s,\lambda)$, where

$$t^*(\theta,\lambda) = A(\theta,\lambda)\exp\left[-B(\theta,\lambda)\tau(\lambda)\right], \tag{5}$$

and θ is either the viewing or the solar zenith angle. The computed diffuse transmittance coefficients $A(\theta,\lambda)$ and $B(\theta,\lambda)$ (Yang & Gordon, 1997) are also stored in the same look-up tables (for each model). As discussed later, SOA interpolates across values of m_i, m_r and ν to essentially give a continuum of models.

2.3. The ocean bio-optical models

The water-leaving reflectance (ρ_w) is provided as a function of the total absorption (a) and backscattering (b_b) coefficients (Gordon et al., 1988). The spectral absorption and backscattering coefficients are further separated into the constituent components plus that of pure sea water:

$$\begin{aligned} a(\lambda) &= a_w(\lambda) + a_{ph}(\lambda) + a_{CDM}(\lambda) \\ a_{CDM}(\lambda) &= a_{CDOM}(\lambda) + a_{dp}(\lambda) \\ b_b(\lambda) &= b_{bw}(\lambda) + b_{bp}(\lambda) \end{aligned} \tag{6}$$

where the subscripts 'w', 'ph', 'CDM', 'CDOM','dp' and 'p' refer to water, phytoplankton, colored detrital material, colored dissolved organic matter, detrital particles, and all particles, respectively. Values of $a_w(\lambda)$ and $b_{bw}(\lambda)$ are known constants (Morel, 1974; Pope & Fry, 1997). The absorption due to detrital particles and colored dissolved organic matter, are combined (into CMD) due to their similar spectral signature. In the GSM model (Garver & Siegel, 1997; Maritorena et al., 2002) all of the optical properties are modeled by three parameters: (1) the absorption coefficient of colored detrital material at 443 nm ($a_{CDM}(443)$); (2) the chlorophyll a concentration C, and (3) the backscattering coefficient of particulate material at 443 nm ($b_{bp}(443)$). Specifically,

$$\begin{aligned} a_{ph}(\lambda) &= Ca^*_{ph}(\lambda), \\ a_{CDM}(\lambda) &= a_{CDM}(443)\ \exp(-S_{CDM}(\lambda-443)) \\ b_{bp}(\lambda) &= b_{bp}(443)(443/\lambda)^{\eta}, \end{aligned} \tag{7}$$

where $a^*_{ph}(\lambda)$ is the chlorophyll a specific absorption coefficient spectrum for phytoplankton, S_{CDM} is the CDM spectral shape parameter and η parameterizes the spectral variation of the particulate backscattering. Given the quantities a^*_{ph}, S_{CDM} and η, the GSM water reflectance model can be represented as

$$\rho'_w(\lambda) = \rho'_w\left(\lambda, C, a_{CDM}(443), b_{bp}(443)\right), \tag{8}$$

where $\rho'_w(\lambda)$ is assumed to be independent of sun or viewing geometry (as in the computation of t^*). Henceforth, a primed symbol indicates a quantity is modeled, as in Eq. (8).

3. Spectral optimization algorithm implementation

We solve for the TOA reflectance by constructing a set of non-linear equations across the eight SeaWiFS bands, and then performing spectral optimization to solve for the seven unknowns C, $a_{CDM}(443)$, $b_{bp}(443)$, m_r, m_i, ν and $\tau(865)$ Eq. (9). Note that because m_r, m_i, ν and $\tau(865)$ specify the aerosol optical depth at all wavelengths, this set specifies ρ'_A at all wavelengths. This forms the modeled counterpart of the expression in Eq. (2).

$$\begin{aligned} &\rho'_{Aw}(\theta_s,\theta_v,\phi,\lambda_i,m_r,m_i,\nu,\tau(865),C,a_{CDM}(443),b_{bp}(443)) \\ &\quad\equiv\rho'_A(\theta_s,\theta_v,\phi,\lambda_i,m_r,m_i,\nu,\tau(865)) + t'_v(\theta_v,\lambda_i,m_r,m_i,\nu,\tau(865)) \\ &\quad\times t'_s(\theta_s,\lambda_i,m_r,m_i,\nu,\tau(865))\times\rho'_w(\lambda,C,a_{CDM}(443),b_{bp}(443)). \end{aligned} \tag{9}$$

The estimation of parameters in Eq. (9) is undertaken as two interdependent steps. First, $\rho_{Aw}(765)$ and $\rho_{Aw}(865)$ and the information contained in the aerosol LUTs are used to provide a constraint on the aerosol models. Then spectral optimization is performed to find *all* the parameters using standard non-linear bounded constrained optimization techniques.

3.1. Selection of aerosol models appropriate to NIR reflectance

Chomko and Gordon (1998, 2001), selected an aerosol model (a particular set of the quantities ν, m_r, and m_i) based on ρ_A at the two NIR bands. Later, Chomko et al. (2003) used a more sensitive approach that involves finding the values of ν and $\tau(865)$ that exactly reproduce $\rho_A(\lambda)$ at both NIR wavelengths (assuming $\rho_w=0$) for each combination of m_r and m_i. We call these $\nu\,(m_r,m_i)$ and $\tau(865,m_r,m_i)$. These are then used to constrain the final optimization. The details of the procedures are provided next.

We simplify notation by using the term NIR where operations are undertaken at *both* 765 and 865 nm wavelengths. The functions $\nu\,(m_r, m_i)$ and $\tau(865,m_r,m_i)$ are estimated at each of the 12 grid points (m_r,m_i) defined in Section 2.2. For this task we find an exact fit between ρ_{Aw} (NIR) and ρ'_{Aw}(NIR), i.e., we solve two equations for two unknowns: ν and τ. This is done through non-linear inversion by minimizing

$$f_{NIR} = \sum_{\lambda_{NIR}}\left\{\rho'_{Aw}(\theta_s,\theta_v,\phi,\lambda_{NIR},m_r,m_i) - \rho_{Aw}(\theta_s,\theta_v,\phi,\lambda_{NIR},\text{measured})\right\}^2. \tag{10}$$

Note that in general ρ_{Aw}(NIR) depends on the water properties as well as the aerosols (this is particularly important in Case 2 waters). As this dependence is unknown *a priori*, the procedure is started assuming ρ'_w(NIR)=0. The order of events begins with selection of a set of starting *candidates* $\nu^{test}(m_r,m_i)$ and $\tau^{test}(865,m_r,m_i)$. Using the LUT's, the quantities $\tau(\lambda,m_r,m_i)$, $t^*(\lambda,m_r,m_i)$ and $\rho'_A(\lambda,m_r,m_i)$ are then interpolated as a function of the *candidate* value $\nu^{test}(m_r,m_i)$ (see Appendix). Finally, the minimization and interpolations are operated iteratively to find $\nu^{opt}(m_r,m_i)$ and $\tau^{opt}(865,m_r,m_i,\nu^{opt})$. At the completion of this procedure, $\nu^{opt}(m_r,m_i)$ and $\tau^{opt}(865,m_r,m_i,\nu^{opt})$, when coupled with m_r, and m_i, exactly (or within the accuracy of the optimization) reproduce ρ_{Aw}(NIR), i.e., $\rho'_A(\text{NIR},m_r,m_i)$.

In Case 2 waters, $t^*(\text{NIR},m_r,m_i,\nu^{opt},\tau^{opt})$ and information on ρ'_w(NIR) are included in the minimization. An estimate of ρ'_w(NIR) is obtained after estimation of the bio-optical properties using Eq. ((8). This part is explained further in Section 3.3. We note that the quantity $\rho'_A(\text{NIR},m_r,m_i,\nu^{test},\tau^{test})$ is center-band while ρ_{Aw}(NIR) is full-band. At these wavelengths the influence of water-vapor and oxygen absorption over the broad spectral bands is significant. We therefore convert ρ_{Aw}

(NIR) from full-band to center-band at *each iteration of the minimization* using the procedure developed by Gordon (1995).

3.2. Retrieval of all parameters

The spectral optimization algorithm uses the six visible (VIS) SeaWiFS bands to estimate five parameters C, $a_{CDM}(443)$, $b_{bp}(443)$, m_r and m_i. Thus, given the functions $\nu^{opt}(m_r,m_i)$ and $\tau^{opt}(865,m_r,m_i,\nu^{opt})$ obtained earlier, minimization of the following function is undertaken

$$f_{VIS}(m_r,m_i,C,a_{CDM}(\lambda_{443}),b_{bp}(\lambda_{443})) \equiv \sum_{\lambda_{VIS}} \left\{ \begin{array}{r} \rho'_{Aw}(\theta_s,\theta_v,\phi,\lambda_{VIS},m_r,m_i,C,a_{CDM}(\lambda_{443}),b_{bp}(\lambda_{443})) \\ -\rho_{Aw}(\theta_s,\theta_v,\phi,\lambda_{VIS},\text{measured}) \end{array} \right\}^2 \quad (11)$$

using the Broyden Fletcher Garbo Shannon (BFGS) non-linear optimization algorithm (Byrd et al., 1995). At each step the iterates from the previous search are used with the Quasi Newton condition. The method has been developed for large scale problems (L) with simple bounds on the variables (B), or L-BFGS-B (Zhu et al., 1997). The SOA now uses Version 2 of Byrd et al. (1995). It is implemented on $f_{VIS}(m_r, m_i, C, a_{CDM}(\lambda_{443}),b_{bp}(\lambda_{443}))$ with the following inequalities:

$$\begin{array}{r} m_i(\min) \le m_i \le m_i(\max), \\ m_r(\min) \le m_r \le m_r(\max), \\ C(\min) \le C \le C(\max), \\ a_{CDM}(\min) \le a_{CDM} \le a_{CDM}(\max), \\ b_{bp}(\min) \le b_{bp} \le b_{bp}(\max). \end{array} \quad (12)$$

where $m_i(\min)=0$, $m_i(\max)=0.04$, $m_r(\min)=1.33$, $m_r(\max)=1.50$, $C(\min)=0.02$ mg m^{-3}, $C(\max)=60.0$ mg m^{-3}, $a_{CDM}(\min)=0.001$ m^{-1}, $a_{CDM}(\max)=1.2$ m^{-1}, $b_{bp}(\min)=0.0001$ m^{-1} and $b_{bp}(\max)=0.1$ m^{-1}. Both a_{CDM} and b_{bp} boundaries correspond to 443 nm. We consider the algorithm to have "failed" if the retrieval yields any of the quantities C, a_{CDM}, or b_{bp} at either the lower or upper boundaries, i.e., if $C=0.02$ mg m^{-3} is retrieved the algorithm failed.

The order of operation begins with selection of a set of starting values for m_r and m_i within the m_r, m_i grid range defined in Section 2.2. Starting values for C, $a_{CDM}(443)$ and $b_{bp}(443)$ are also input to a forward GSM model to determine $\rho'_w(VIS)$. Partial derivatives (in m_r and m_i) required for the optimization are then calculated for candidates $k(\lambda,m_r,m_i)$, $\tau(865,m_r,m_i)$, $\rho'_A(VIS,m_r,m_i)$, $A(VIS,\theta,m_r,m_i)$ and $B(VIS,\theta,m_r,m_i)$ determined in Section 3.1 and $\rho'_w(VIS)$. Rectangular grid bivariate interpolation (in m_r and m_i) is then used to interpolate all values and partials for the input starting values of m_r and m_i. For interpolation in the m_i direction, we interpolate on $m_i^{1/4}$ rather than m_i itself, as ρ'_{Aw} is closer to linearity as a function of $m_i^{1/4}$. We also interpolate directly on m_r since ρ'_{Aw} is not entirely linear but is relatively flat in this direction. No interpolation is required for ρ'_w as an analytical formulation (GSM) is used. Once again the equivalence $k(\lambda)/k(865)=\tau(\lambda)/\tau(865)$ is used to determine $\tau(VIS)$ from $\tau(865)$, and $\tau(VIS)$, $A(VIS,\theta)$ and $B(VIS,\theta)$ allow estimation of $t^*(VIS)$, all in m_r, m_i.

The derived $\rho'_{Aw}(VIS)$ and all partials are then tested in the optimization to search for improved *candidates* C, $a_{CDM}(443)$, $b_{bp}(443)$, m_r and m_i given the objective function (11). The process requires tracking of the status of all parameters at each iteration number j of the optimization, i.e., the output triggered by the completion of a search at a particular step. The relative error f^j_{lsq}, expressed as a percentage, is obtained for the minimization function (11) and determined at each iteration j performed by L-BFGS-B in SOA and for each pixel. The procedure is stopped when

$$\frac{f^j_{lsq}-f^{j+1}_{lsq}}{\max\left\{|f^j_{lsq}|,|f^{j+1}_{lsq}|,1\right\}} \le s_{tol} \quad (13)$$

where a lower s_{tol} (stop tolerance) results in higher precision retrievals. i.e., a closer match up between $\rho'_{Aw}(VIS)$ and $\rho_{Aw}(VIS)$. At this point all retrieved parameters are deemed optimal. Setting s_{tol} to 2×10^{-7} results in accuracy of 0.1 to 3.0% between ρ'_{Aw} and ρ_{Aw} at all six visible SeaWiFS bands. Note that this does not guarantee that ρ_w is of the same accuracy. This would require an almost prefect retrieval of ρ_A and t^* at each wavelength.

To the best of our knowledge, the quasi-Newton class methods do not guarantee, in general, a convergence to a minimum for the specified objective function. Therefore, to increase the likelihood of convergence in Case 2 waters, we run the SOA for six different sets of starting values of C, $a_{CDM}(443)$ and $b_{bp}(443)$ and select the combination that gives the highest accuracy (lowest f^j_{lsq}) after 15 iterations. Here, starting C is always low and $a_{CDM}(443)$ and $b_{bp}(443)$ covary within their full range. On most occasions the choice of starting values actually has no effect on the retrieval. It does however lead to a small increase in retrieval rate during the rare situation where the optimization gets 'stuck' (and therefore "fails") at one of the boundaries given in the inequalities (12). The SOA is then restarted and iterates until s_{tol} is of the order of 2×10^{-7}. In this procedure we again apply a correction to the aerosol reflectance at each j to handle the fact that modeled data is center-band while measured data is full-band. In this instance measured $\rho_A(VIS)$ is not known *a priori* (because $\rho_w(VIS)$ is not negligible), therefore we apply a center-band to full-band correction to the modeled value $\rho'_A(VIS,m_r,m_i)$.

As a post-processing step, final values for ν, τ (λ) and $\omega_0(\lambda)$ are determined using both bivariate interpolation (in *optimal* m_r and m_i) and the information at gridded m_r and m_i determined in the Appendix. In effect, all seven parameters C, $a_{CDM}(443)$, $b_{bp}(443)$, ν, $\tau(865)$, m_r and m_i are optimized, and ω_0 determined by interpolation, using the eight spectral bands of SeaWiFS and the constraint that $\rho'_{Aw}=\rho_{Aw}$ in the NIR i.e. the whole scheme provides aerosol and ocean parameters simultaneously.

3.3. Implementation in Case 2 waters

Both Gordon and Wang (1994) and Chomko et al. (2003) assume that $\rho_{Aw}(NIR)=\rho_A(NIR)$ in Case 1 waters. In many Case 2 waters the actual NIR water leaving reflectance is non-zero as a result of backscatter from phytoplankton pigment and detritus (Siegel et al., 2000) as well as suspended sediments. To account for this we iterate SOA in the following manner. The algorithm assumes $\rho'_A(NIR)=\rho'_{Aw}(NIR)$ to determine an initial estimate of $\nu(m_r,m_i)$ and $\tau(NIR,m_r,m_i)$. Estimates of $A(NIR,\theta,m_r,m_i)$ and $B(NIR,\theta,m_r,m_i)$ provide an initial estimate of $t^*(NIR,m_r,m_i)$ from Eq. (5). Subsequent operation of the minimization in function (11) provides estimates of C, $a_{CDM}(443)$ and $b_{bp}(443)$ from which an estimate of $\rho'_w(NIR)$ is obtained. Ignoring the m_r and m_i dependency for brevity, the estimate of $t^*\rho'_w(NIR)$ is then subtracted from the total reflectance to form the corrected reflectance, i.e.,

$$\rho^{(Corrected)}_{Aw}(NIR)=\rho_t(NIR)-\rho_r(NIR)-t^*(NIR)\rho'_w(NIR), \quad (14)$$

and the updated $\rho^{(Corrected)}_{Aw}(NIR)$ is used to initiate a new optimization, i.e., improved estimates of $\nu(m_r,m_i)$ and $\tau(865,m_r,m_i)$ and subsequent calculation of new water parameters. The procedure iterates until the magnitude of $\rho_w(865)$ (or its difference across consecutive Case 2 loops, namely delta $\rho_w(865)$) falls below 0.0001. This generally increases the processing time of the SOA to an order of magnitude more than the standard algorithm.

4. Model performance

The SOA model presented above is sufficiently complex that it is nearly impossible to understand how well it might perform in a given scenario. Thus, to test the SOA performance, we developed an independent synthetic data set for comparison. Aerosol reflectance ρ_A (λ) was generated using two separate models: the coastal Gordon and Wang (1994) model at 50% relative humidity, C50, and the moderately

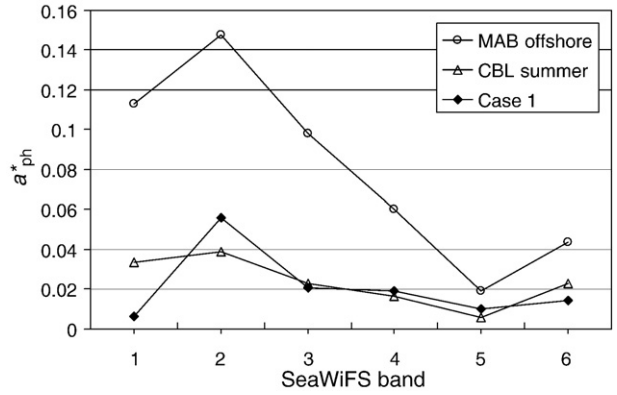

Fig. 1. Quantity $a^*_{ph}(\lambda)$ for Chesapeake lower bay (summer) and the Middle Atlantic Bight offshore regions, from Magnuson et al. (2004). Case 1 is also given from Maritorena et al. (2002).

absorbing urban model at 90% relative humidity, U90. The C50 model displays moderate wavelength dependent Angström exponent (0.73–0.79) and ω_0 (0.97–0.98). Respective values for the U90 model are (1.09–1.21) and (0.82–0.84). In both models the aerosol is vertically mixed from 0 to 2 km. It should be noted that these size distributions are the sum of two log-normal distributions (Gordon and Wang, 1994). Such distributions are sometimes, but not always well approximated by the Junge power-law size distribution (for examples, see Chomko and Gordon (1998), Fig. 3).

Simulated data were constructed at geometry of $\theta_s = 30.0°$, $\theta_v = 20.87°$, and $\phi = 130.0°$, and six values of aerosol optical depth at 865 nm, $\tau(865) =$ 0.01, 0.03, 0.05, 0.1, 0.2 and 0.4. Values of diffuse transmittance coefficients $A(\lambda)$, $B(\lambda)$ at both θ_s and θ_v were also computed from the same model. Information from the extinction coefficient $k(\lambda)$, the proportionality between $k(\lambda)$ and $\tau(\lambda)$, and the formulation of Eq. (5) determined corresponding diffuse transmittance $t^*(\lambda)$.

Two sets of bio-optical coefficients CBL and MAB were used in the generation of synthetic ρ_w. In-situ measurements in the Chesapeake Bay area were used to generate CBL and MAB values of the parameter S_{CDM} of 0.0133 and 0.01646 respectively (Magnuson et al., 2004). The quantity $a^*_{ph}(\lambda)$ obtained in the same study is significantly higher in MAB than CBL, and both differ appreciably from Maritorena et al. (2002) Case 1 values at 412 and 443 nm (Fig. 1). The parameter η was not obtained in the Magnuson study. Instead, backscattering coefficient measurements have been recorded in the *middle* bay at the mouth of the Potomac River (2 samples) and *upper* bay (9 samples) at 450, 550 and 650 nm (Tzortziou et al., 2006; Gallegos, 2006). Quantity η was then derived using quadratic interpolation and the expression for b_{bp} in Eq. (7).

For MAB we elected a similar value of 1.0 as no *in situ* backscattering measurements were available in this region. We note that Case 1 GSM η is also approximately 1.0. The choice of CBL and MAB regions for testing in this study was based on the fact that $a^*_{ph}(\lambda)$ differed appreciably between regions and the relative magnitudes of the coefficients within each region are realistic, determined from relatively large *in situ* data sets. The possible 0–20% error in MAB η is therefore considered irrelevant for the purposes of this study. To generate synthetic $\rho_w(\lambda)$, the GSM model was operated at 80 different combinations of C (0.1, 0.5, 1.0, 10.0 mg m^{-3}), $a_{CDM}(443)$ (0.003, 0.01, 0.1, 0.5, 1.0 m^{-1}) and $b_{bp}(443)$ (0.001, 0.003, 0.01, 0.03 m^{-1}) at both CBL and MAB bio-optical coefficient settings (as opposed to the GSM Case 1 settings), for a total of 160 different spectra of $\rho_w(\lambda)$.

All GSM water $\rho_w(\lambda)$'s were then combined with each set of aerosol data produced by C50 and U90 at each of the 6 values of $\tau(865)$. This created a total data set that consists of 80 water combinations at six aerosol optical depths for two different sets of bio-optical coefficients and two aerosol models, i.e., 1920 sets of synthetic $\rho_A(\lambda) + t^*\rho_w(\lambda)$.

4.1. Aerosol reflectance

The SOA, implemented as described in Section 3, was operated in Case 2 mode across all 1920 combinations of synthetic $\rho_A(\lambda) + t^*\rho_w(\lambda)$ described previously. That is, we substitute for $\rho_{Aw}(\lambda)$ in function (11) and, initially, use the *same* GSM parameters in the retrieval as those used to generate the synthetic data. All configurations in synthetic and

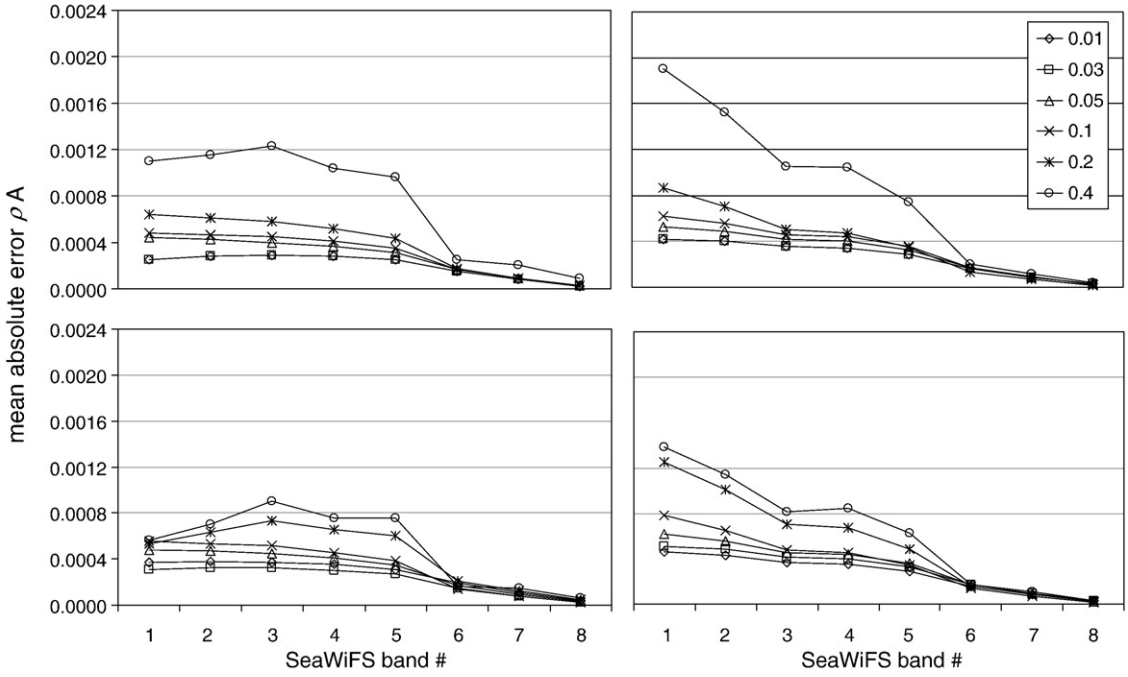

Fig. 2. Comparison of synthetic $\rho_A(\lambda)$ and SOA $\rho'_A(\lambda)$ for CBL (top) and MAB (bottom) at 6 legend optical depths $\tau(865)$. The left and right graphs are for synthetic C50 and U90 respectively. Each data point represents the mean *absolute* difference between $\rho_A(\lambda)$ and $\rho'_A(\lambda)$ for 80 different GSM input combinations of C, $a_{CDM}(443)$ and $b_{bp}(443)$ at both CBL and MAB.

SOA were the same (e.g., geometry, Rayleigh component etc.) and all data were band centered.

A high precision aerosol correction is required for robust operation of ocean color data given the relatively large contribution by aerosol to the total radiance measured at the satellite sensor. To determine the quality of the estimated aerosol component, the absolute error between generated $\rho_A(\lambda)$ from both C50 and U90, and $\rho'_A(\lambda)$ from the SOA, was first determined at each combination of C, $a_{CDM}(443)$, $b_{bp}(443)$ and $\tau(865)$. Fig. 2 illustrates the resulting mean *absolute* error for a total of 80 water combinations averaged at each optical depth for both CBL (top) and MAB (bottom), and both C50 (left) and U90 (right). Results show that SOA $\rho'_A(\lambda)$ performs remarkably using C50 in both CBL and MAB for all but $\tau(865)=0.4$ in CBL. Using U90, the error is increased at higher optical depths in both regions. This shows that the aerosol error may be significant (approaching an error >0.001) if the optical depth is high (≥0.2 at 865 nm) and the aerosol is absorbing. Interestingly, the standard deviation in the mean absolute error in $\rho'_A(\lambda)$ is roughly equal to the mean absolute error itself. Thus for any particular case, the error in $\rho'_A(\lambda)$ could likely range from zero to approximately double that shown in Fig. 2.

4.2. Chlorophyll and CDM performance

In this section we explore the range and performance of the SOA. We calculate ratios (C-SOA/C-synthetic) and ($a_{CDM}(443)$-SOA/$a_{CDM}(443)$-synthetic) at both CBL and MAB. The ratios are then ordered from lowest to highest and presented in Fig. 3. The upper-left graph corresponds to C, upper-right corresponds to $a_{CDM}(443)$. Results in both top graphs are shown for CBL and MAB at $\tau(865)$ of 0.1 (points) and C50. Also shown are CBL at extreme $\tau(865)$ of 0.01 and 0.4 (lines only) to illustrate the effect of variation in aerosol thickness.

For the C match up, SOA is precise for approximately 50 of the 80 combinations in both CBL and MAB at $\tau(865)$ of 0.1 using C50. The vast majority of the 30 poor match ups occur for combinations of $a_{CDM}(443)$ or C that do not covary positively with $b_{bp}(443)$. A further comparison of data at the extreme optical depths show a small increase in SOA precision at low $\tau(865)$ and vice versa at high. Note that more good retrievals are obtained with the MAB than the CBL parameters. This is likely due to the much larger $a^*_{ph}(\lambda)$ for MAB resulting in a higher sensitivity of $\rho_w(\lambda)$ to C.

To try to understand how the retrieval failures occur, the lower left graph in Fig. 3 is a mapping of $f(a,b_{bp})$ to CBL C at $\tau(865)=0.1$ given in the upper left graph where

$$f(a,b_{bp}) = \left(\frac{a_{CDM}(443)}{a_{ph}(443)+a_{CDM}(443)}\right)^2 (b_{bp}(443)u)^{-1} \quad (15)$$

The numerator in Eq. (15) is the fraction of the total absorption at 443 nm (less water) due to CDM. In the denominator the factor u is a magnification term for b_{bp} and set to 10^2 in this analysis. The results in Fig. 3 indicate a strong relationship between $f(a,b_{bp})$ (lower left graph) and C retrieval (upper left graph) with $f>1.0$ indicating a high chance of SOA failure. This provides a semi-quantitative indicator of the chance of SOA success in a given situation. For example, if the water absorption at 443 nm is 80% dominated by CDM and 20% phytoplankton, then the corresponding $b_{bp}(443)$ needs to be greater than approximately 0.0064 for good C retrieval. The fact that we need to square the CDM fraction term in Eq. (15) implies that the spectral shape of $\rho_w(\lambda)$ is slightly more important for SOA operation than its magnitude as represented by b_{bp}.

For the $a_{CDM}(443)$ match up, the frequency and magnitude of good retrievals is actually very similar to the C retrievals for each of the

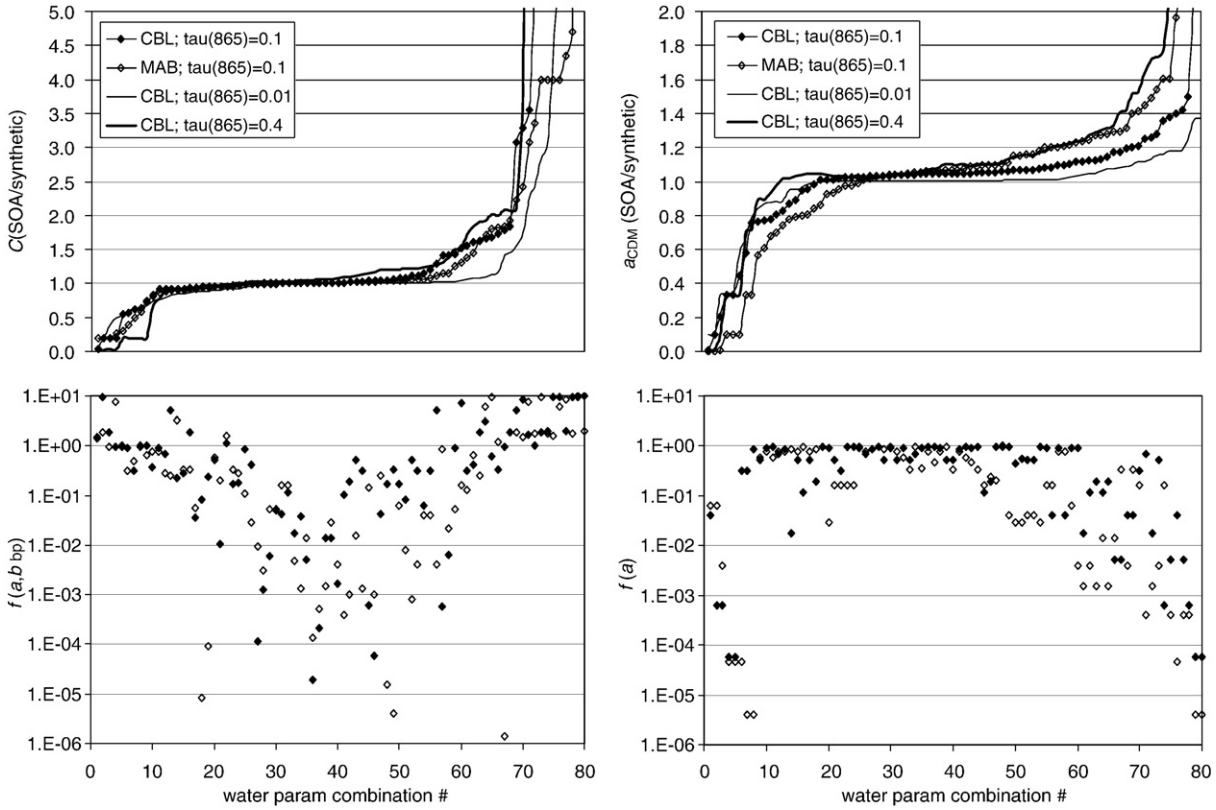

Fig. 3. Ordered ratios of C-SOA and C-synthetic (top-left) and $a_{CDM}(443)$-SOA and $a_{CDM}(443)$-synthetic (top right) at 80 combinations of C, $a_{CDM}(443)$ and $b_{bp}(443)$ using aerosol model C50. The legend shows two conditions of bio-optical region (CBL, MAB) at $\tau(865)=0.1$. Also shown are CBL at $\tau(865)=0.01$ and 0.4 using C50. The bottom graphs (left to right) show $f(a,b_{bp})$ and $f(a)$ for both MAB and CBL, described in the text, at both MAB and CBL given in the upper graphs at $\tau(865)=0.1$.

given scenarios. However, note that the order of combinations C, a_{CDM}(443), b_{bp}(443) in the abscissa of the upper left C graph is different from the upper right a_{CDM}(443) graph. Thus, some of the good CDM retrievals actually occur for poor C retrievals and vice versa. This is exemplified by the moderate relationship between function $f(a)$ (lower right graph) and SOA a_{CDM}(443) retrieval (upper right graph) given in Fig. 3 where $f(a)$ is now only the numerator in Eq. (15). It shows that as the proportion of CDM in the water column increases (relative to phytoplankton), then the precision of SOA for retrieval of a_{CDM}(443) improves. (Inclusion of the b_{bp} term here actually weakened the relationship.) This bodes well for using of the SOA for a_{CDM}(443) estimation, under similar aerosol conditions, in waters dominated by a_{CDM}(443) irrespective of the magnitude of ρ_w, as long as it is not too low compared to ρ_A (see next section).

4.3. Water reflectance

Fig. 4 illustrates SOA $\rho'_w(\lambda)$ for 16 water parameter combinations (from 80) for CBL (left) and MAB (right) at synthetic C of 0.1 (top) and 10.0 mg m^{-3} (bottom). Within each graph are eight curves corresponding to synthetic $a_{CDM}(443)=0.003$ and 1.0 m^{-1} at $b_{bp}(443)=0.001$, 0.005, 0.01 and 0.03 m^{-1}. The solid lines are successful SOA retrievals; dashed lines are SOA failure. Success is defined as an error in the SOA retrieved $C<30\%$. Failure occurs when the error is $>30\%$ and is referred to as "C-failure." The aerosol $\tau(865)=0.1$ using C50 in all data.

The most obvious observation regarding Fig. 4 is the fact that all C-failures are in waters with low $\rho'_w(\lambda)$ in the visible (i.e., dark waters), a manifestation of the obvious fact that when the water signal becomes too low, it cannot be accurately retrieved from $\rho_t(\lambda)$. This usually (but not always) occurs when the water reflectance falls to ~10^{-3} in the blue which is near to the expected error in $\rho'_A(\lambda)$. As discussed below, the C-failures that do not follow this observation, i.e., CBL at low C, result from the relative insensitivity of the water reflectance to C because of the low values of a^*_{ph} in the blue. In accordance with the relationship in Eq. (15), a combination of low b_{bp} and/or relatively high CDM results in failure. Furthermore, an interesting trend exists with all synthetic bio-optical combinations in this study: a better C retrieval is obtained when CDM and b_{bp} once again covary positively. Put simply, as CDM increases then so must b_{bp}, otherwise the water becomes too dark. However, this trend is also dependent on the bio-optical coefficients. For example, at high C, SOA performance indicates that the covariation restriction between a_{CDM}(443) and b_{bp}(443) can be relaxed for CBL data, while at low C the covariation is paramount because C has a much smaller affect on $\rho_w(\lambda)$ than in the MAB. This inversion in the performance (for CBL low C and high a_{CDM}(443) always results in failure, but not at high C, while in the MAB the reverse is observed) is a direct result of the relative size of $a^*_{ph}(\lambda)$ in each region. Examination of the error in the retrieved ρ_w spectra indicates that most successful retrievals display an error that is nearly independent of wavelength and less than or approximately equal to 10–20% across most of the visible spectrum. Some C-failures also have retrievals of $\rho_w(\lambda)$ at similar relative accuracies but fail because of the insensitivity of $\rho_w(\lambda)$ to C.

4.4. Bio-optical model coefficient error

At this point it is important to remember that $\rho_w(\lambda)$ is determined by the total absorption and backscattering coefficients. If atmospheric correction were perfect, then $a(\lambda)$ and $b_b(\lambda)$ would be determined precisely. The bio-optical model does the portioning of absorption coefficient between that due to C and that due to CDM. Thus, even if $\rho_w(\lambda)$ is error free, error in the bio-optical model coefficients (S_{CDM}, η and a^*_{ph}) used in the retrieval will cause error in the retrieved bio-optical parameters. This is exacerbated in the SOA, because *all* of the parameters are retrieved simultaneously, so error in one bio-optical parameter can influence retrieval of *all* parameters, including those relating to the atmosphere.

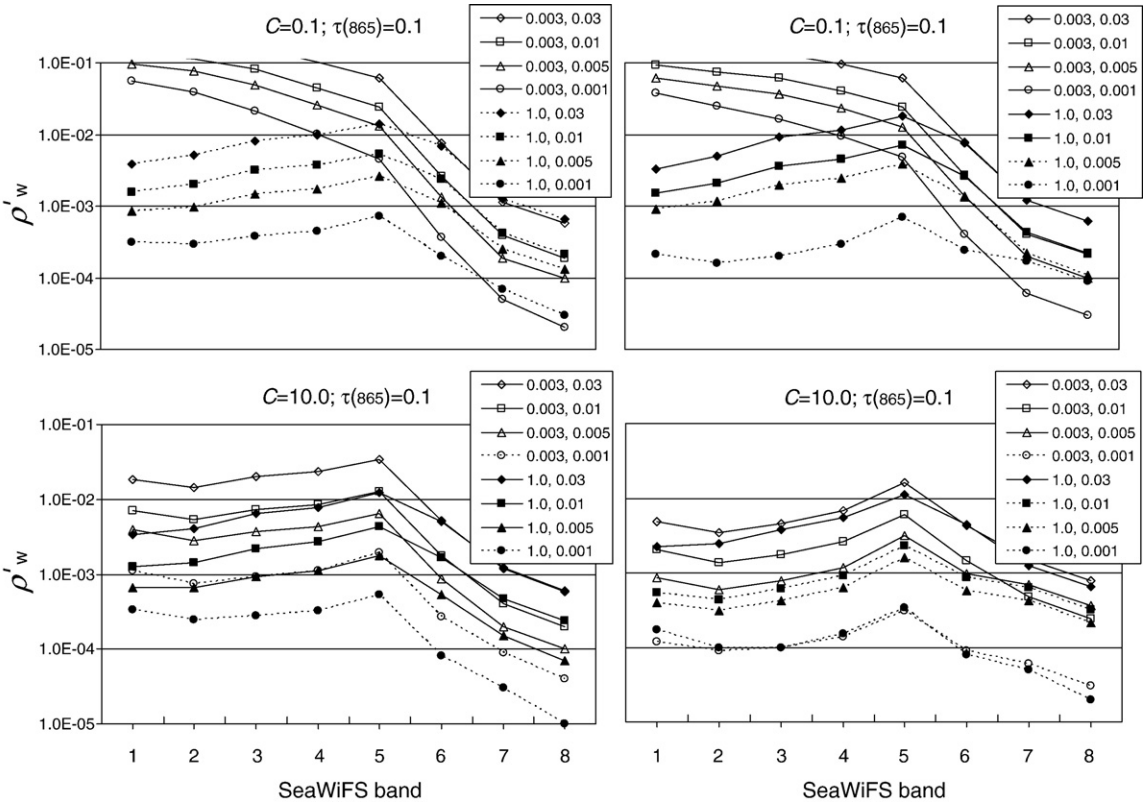

Fig. 4. SOA $\rho'_w(\lambda)$ for CBL (left col) and MAB (right col) and synthetic $C=0.1$ and 10.0 mg m^{-3} (top to bottom rows respectively). Each graph presents 8 curves corresponding to synthetic $a_{CDM}(443)=0.003$ and 1.0 m^{-1} (first entry in the legend box) each at $b_{bp}(443)$ of 0.001, 0.005, 0.01 and 0.03 m^{-1} (second entry in the legend box). The solid lines are successful SOA retrievals; dashed lines are SOA failure at 30% tolerance. Aerosol $\tau(865)=0.1$ using C50 in all data.

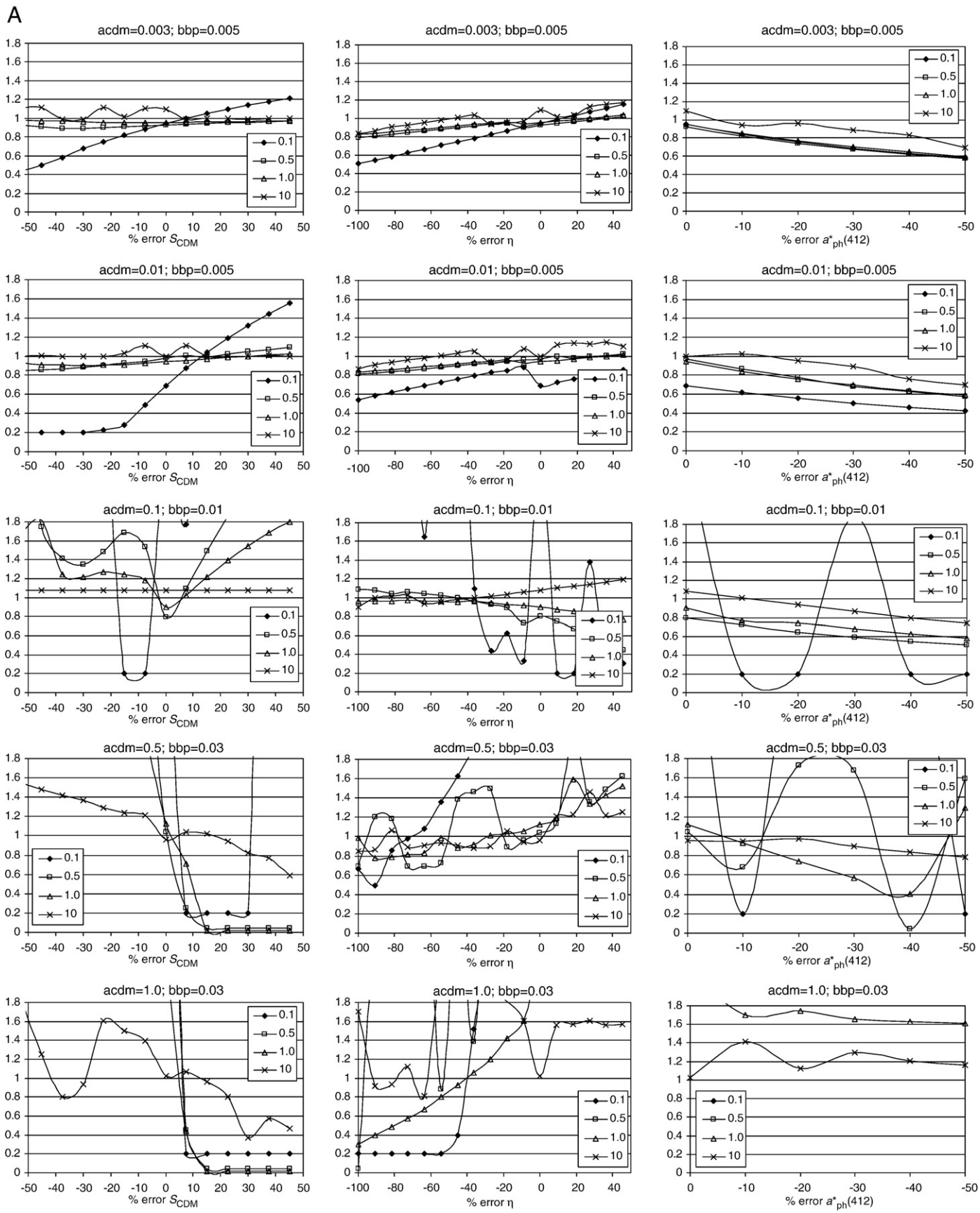

Fig. 5. A) Ratio of SOA retrieved *C* to synthetic *C* (*y*-axis) and its sensitivity to GSM bio-optical coefficients (*x*-axis) in CBL. Each column (l–r) represents sensitivity to S_{CDM}, η and a^*_{ph} (412) respectively. Five GSM input combinations of $a_{CDM}(443)$ and $b_{bp}(443)$ are tested (rows t–b), each at four values of input *C* (legend values). Results are shown for $\tau(865)$ of 0.1 and aerosol model C50. B) Ratio of SOA retrieved *C* to synthetic *C* (*y*-axis) and its sensitivity to GSM bio-optical coefficients (*x*-axis) in CBL. Water configuration is the same as for Fig. 5A, quantity $\tau(865)=0.1$ and the aerosol model = U90.

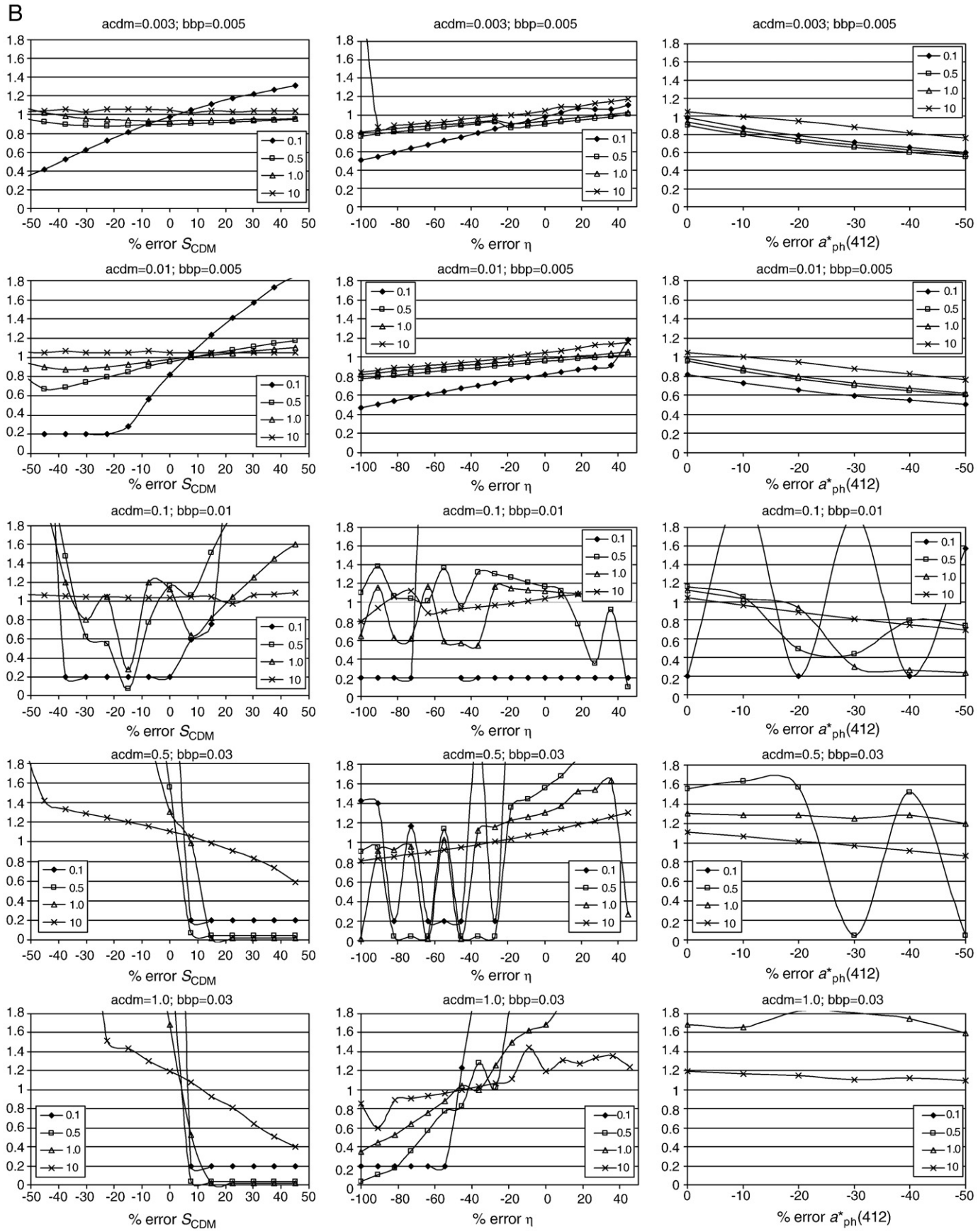

Fig. 5 (*continued*).

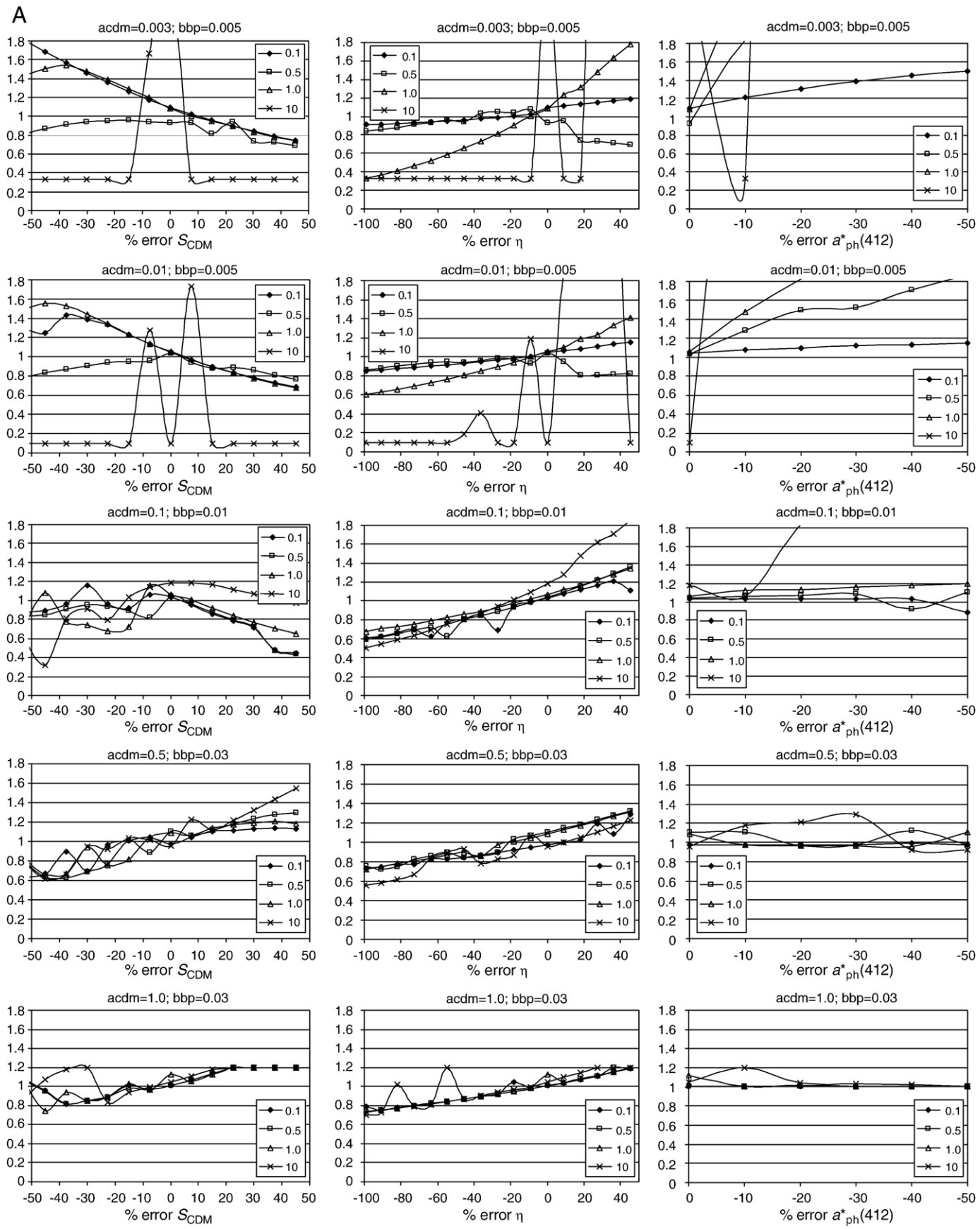

Fig. 6. (A) Ratio of SOA retrieved $a_{CDM}(443)$ to synthetic $a_{CDM}(443)$ (y-axis) and its sensitivity to GSM bio-optical coefficients (x-axis) in CBL. Each column (l–r) represents sensitivity to S_{CDM}, η and $a^*_{ph}(412)$ respectively. Five GSM input combinations of $a_{CDM}(443)$ and $b_{bp}(443)$ are tested (rows t–b), each at four input values of C (legend values). Results are shown for $\tau(865)$ of 0.1 and aerosol model C50. B) Ratio of SOA retrieved $a_{CDM}(443)$ to synthetic $a_{CDM}(443)$ (y-axis) and its sensitivity to GSM bio-optical coefficients (x-axis) in CBL. Water configuration is the same as for Fig. 6A, quantity $\tau(865)=0.1$ and the aerosol model=U90.

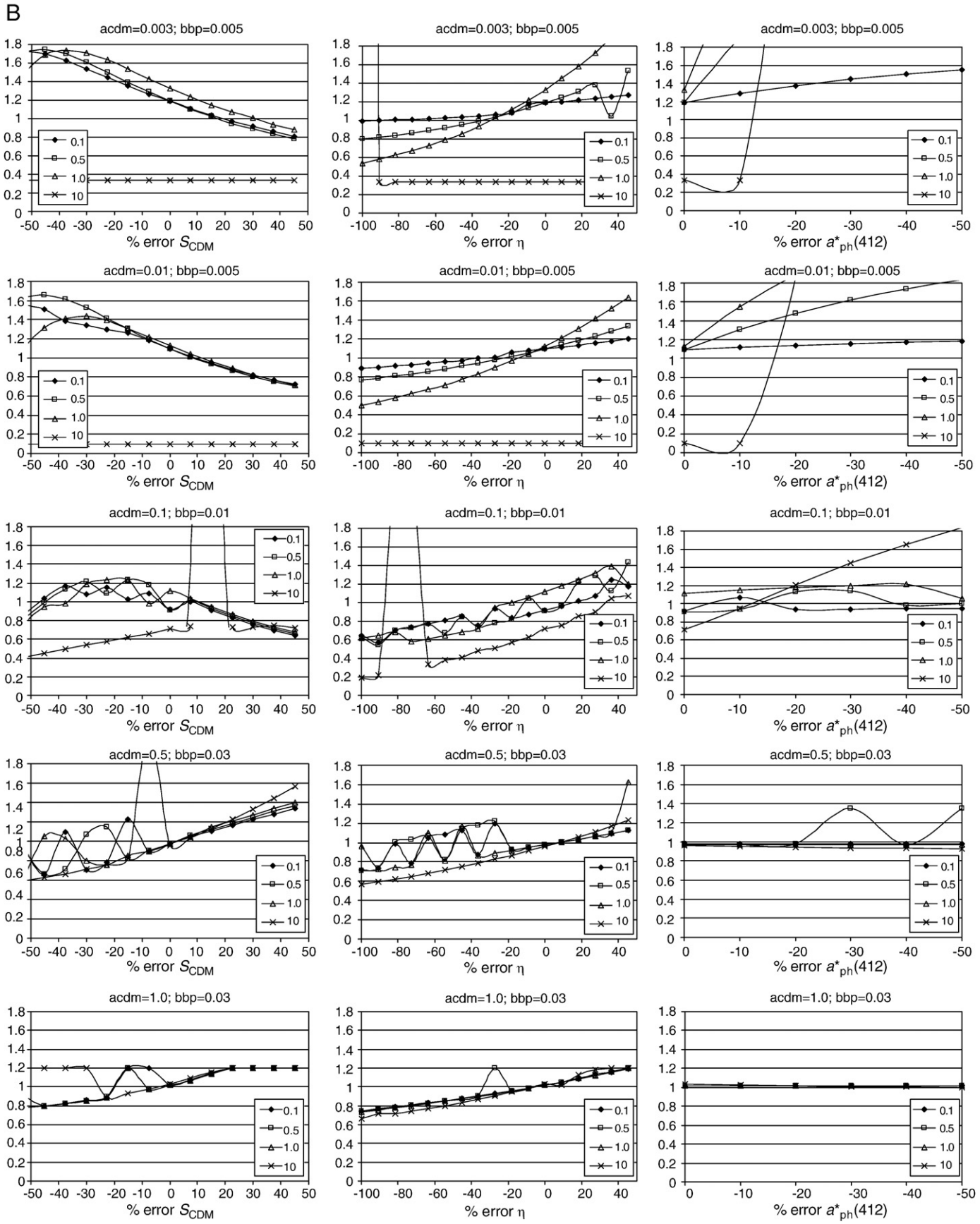

Fig. 6 (*continued*).

Table 1
Water parameter combinations and their associated index reference values c1 to c8

Spectra #	C	$a_{CDM}(443)$	$b_{bp}(443)$	$f(a,b_{bp})$
c1	0.5	0.003	0.005	0.0552
c2	**0.5**	**0.003**	**0.01**	**0.0276**
c3	1.0	0.01	0.005	0.1243
c4	**1.0**	**0.01**	**0.01**	**0.0622**
c5	1.0	0.1	0.01	0.5908
c6	**1.0**	**0.1**	**0.03**	**0.1969**
c7	10	0.1	0.01	0.0622
c8	**10**	**0.1**	**0.03**	**0.0207**

Quantity $f(a,b_{bp})$ is from Eq. (15).

Here we explore the SOA-retrieval's dependence on GSM bio-optical model coefficient error by systematically varying the bio-optical coefficients S_{CDM}, η and $a^*_{ph}(412)$ used in the SOA retrievals from those used to generate the synthetic data. This is undertaken to give the user a sense of the error that can be expected using SOA with uncertain coefficients. The decision to vary quantity $a^*_{ph}(412)$ was motivated by the possibility that its value can confuse the separation of C and CDM, as a_{CDM} is largest at 412 nm.

4.4.1. Effect of bio-optical coefficient error on SOA chlorophyll retrieval

In this section we introduce GSM model coefficient error into the SOA retrieval code and compare synthetic and SOA-retrieved C. Fig. 5A corresponds to CBL using aerosol model C50, and Fig. 5B corresponds to CBL using aerosol model U90 (to assess performance in the presence of a moderately absorbing aerosol). The ordinate axis in each graph corresponds to the ratio of SOA-retrieved C to the (correct) synthetic C. Five different combinations of $a_{CDM}(443)$ and $b_{bp}(443)$ were selected for testing and correspond to the five rows (t–b) in the figures. Respectively, the tested combinations are $a_{CDM}(443)$= 0.003 and $b_{bp}(443)$=0.005, $a_{CDM}(443)$=0.01 and $b_{bp}(443)$=0.005, $a_{CDM}(443)$=0.1 and $b_{bp}(443)$=0.01, $a_{CDM}(443)$=0.5 and $b_{bp}(443)$= 0.03, and $a_{CDM}(443)$=1.0 and $b_{bp}(443)$=0.03. All units are per meter. The selected combinations positively covary as mentioned in Section 4.3. The three columns in Fig. 5A and B represent, from left to right, graphs whose abscissa is the % variation in the bio-optical coefficients S_{CDM}, η and $a^*_{ph}(412)$ respectively in the SOA. The 0% value is the correct respective model, i.e., the value that was used to create the synthetic data. Each graph contains four curves corresponding to synthetic C=0.1, 0.5, 1.0 and 10.0 mg m^{-3}. $\tau(865)$ is 0.1 throughout.

The first two rows in Fig. 5A and B correspond roughly to Case 1 waters ($a_{CDM}(443)\leq 0.01$ m^{-1}). We see excellent retrieval of C when there is no bio-optical model error for both C50 and U90. The addition of bio-optical model error at low $a_{CDM}(443)$ has minor effect except for S_{CDM} at low C. The low-C case shows some curious effects. The second row, left panels of both figures shows that error in S_{CDM} can cause total failure of the algorithm (Note: when C=0.1 mg m^{-3}, the SOA-synthetic ratio of 0.2 corresponds to a retrieval of 0.02 mg m^{-3}, which indicates algorithm failure, i.e., the lower boundary on the retrieved C in Eq. (12)). In addition, error in η can cause unexpected behavior in the retrieved C (Fig. 5A, second row, center panel). These effects are due to the interplay between the water and atmospheric parts of the algorithm, as variations in S_{CDM} and η produce significant variations is the spectral shape of $\rho_w(\lambda)$ for waters in which the reflectance is large enough to be comparable with $\rho_A(\lambda)$ in the blue. In general, at low $a_{CDM}(443)$ the SOA is least sensitive to the bio-optical coefficients (except for S_{CDM} at low C) relative to higher values of $a_{CDM}(443)$, with the extra caveat that $b_{bp}(443)$ must be at least 0.003 m^{-1}.

The centre row of each figure corresponds to high $a_{CDM}(443)$=0.1 m^{-1}. Results for both C50 and U90 are again very similar, showing failure or high sensitivity to coefficient error for low-C values and good performance and low sensitivity to coefficient error for high-C values. As expected, increasing $a_{CDM}(443)$ to very high values (last two rows Fig. 5A and B) leads to a progressive deterioration in the retrieval of lower values of C, where the absorption by CDM overshadows that due to C.

The results in this section illustrate the interplay between bio-optical model error and the SOA limitations as described in Section 4.2 for water dominated by CDM and/or low b_{bp}. Examples are the simulations at very high $a_{CDM}(443)\geq 0.5$ m^{-1} given S_{CDM} error (left column, last two rows of both figures). In each graph the results show, as one would expect, that *any* error in S_{CDM} lowers the effective range of SOA operation in waters where CDM is very high.

An identical set of simulations were carried out for waters for which the MAB values of $a^*_{ph}(\lambda)$ would be appropriate (not shown). The results are similar to those provided in Fig. 5A and B, but with important differences. Because lower values of C produce significantly more absorption in the MAB than in the CBL case, the SOA performs better at lower values of C in the MAB than in the CBL for each case. As $a_{CDM}(443)$ increases, the degradation in the quality of the retrieved C occurs at higher values of $a_{CDM}(443)$ in the MAB than in the CBL.

Summarizing, within the context of the parameter regimes studied here, where there is a positive correlation between $a_{CDM}(443)$ and b_{bp}, the simulations show that with a ±10% error in S_{CDM}, reasonable retrievals of C are usually obtained for $C\geq 0.5$ mg m^{-3} and $a_{CDM}(443)\leq 0.1$ m^{-1} in the CBL, and for $C\geq 0.1$ mg m^{-3} and $a_{CDM}(443)\leq 0.5$ m^{-1} in the MAB. Similarly, a ±10% variation in η does not disrupt good retrievals when $C\geq 0.5$ mg m^{-3} for most $a_{CDM}(443) - b_{bp}$ combinations.

4.4.2. Effect of bio-optical coefficient error on SOA $a_{CDM}(443)$ retrieval

An important aspect of the SOA is the possibility of the retrieval of detrital absorption. In Fig. 6A and B, we provide the error in retrieval of $a_{CDM}(443)$ induced by bio-optical model error in CBL using aerosol model C50 and U90, respectively. Although absorbing aerosol and CDM absorption produce similar variations in ρ_{Aw} in the blue, the effect of switching from C50 to U90 is virtually non-noticeable at this optical depth $\tau(865)$=0.1, except at low $a_{CDM}(443)$ (top row). As with the C retrievals, this trend may differ at very high optical depths given the larger error in the aerosol retrieval for U90 compared to C50 (Fig. 2).

Specifically, results show that for $a_{CDM}(443)\leq 0.01$ m^{-1}, the $a_{CDM}(443)$ retrieval is highly sensitive to error in $a^*_{ph}(412)$. Sensitivity to S_{CDM}, although less, is also significant. This is to be expected as these coefficients largely determine the relative proportions of a_{CDM} and a_{ph} to the total absorption at blue wavelengths. Hence, at low $a_{CDM}(443)$, the $a_{CDM}(443)$ retrieval is also poor at very high C. Under these conditions we are attempting to optimize a very low CDM signal versus phytoplankton. As we increase $a_{CDM}(443)$ the retrieval rapidly improves and becomes relatively insensitive to small errors in the coefficients. For $a_{CDM}(443)\geq 0.1$ m^{-1}, the error in the retrieved $a_{CDM}(443)$ will usually be less than 20% as long as C is not too large. Although not shown here, $a_{CDM}(443)$ also shows a weak dependence

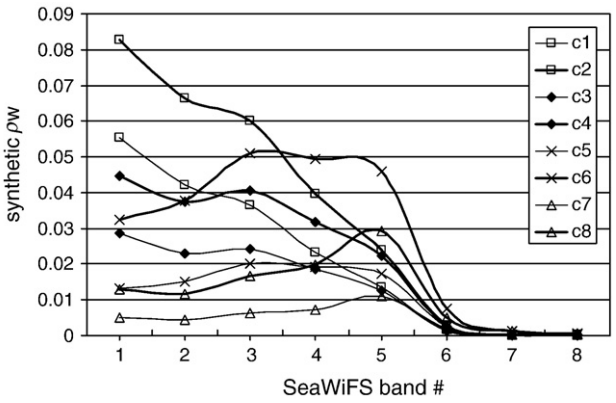

Fig. 7. GSM CBL synthetic ρ_w spectra for c1 to c8 in Table 1. Spectra numbers c1 and c2, c3 and c4 etc. are ordered pairs of increasing $b_{bp}(443)$. The high b_{bp} spectra are given in bold.

on bio-optical region with results slightly improved for CBL due to a decrease in $a^*_{ph}(\lambda)$ compared to that for MAB.

4.4.3. SOA chlorophyll-retrieval sensitivity to τ and b_{bp}

In Section 4.3 we discussed the effect of low b_{bp} on optimization performance at $\tau(865)$ of 0.1. To conclude the discussion of the influence of bio-optical model error, we now include in the analysis a more complete investigation of the effect of $\tau(865)$ and the concomitant role of $b_{bp}(443)$. This is undertaken to show how the interplay between the relative magnitudes of both $\rho_A(\lambda)$ (controlled by $\tau(865)$) and $\rho_w(\lambda)$ (controlled by $b_{bp}(443)$) can affect the SOA retrievals.

To facilitate this, we operate SOA with C50 and select four CBL spectra of synthetic ρ_w at both low and high $b_{bp}(443)$, a total of eight spectra. For notation, we label the spectra c1 to c8 and also give the corresponding values of synthetic C, $a_{CDM}(443)$ and $b_{bp}(443)$ in Table 1, with high b_{bp} combinations in bold. The associated ρ_w spectra are given in Fig. 7 with high b_{bp} spectra again in bold. We operate SOA as before using input t^* and $\rho_A(\lambda)$ to generate optimal $\rho'_{Aw}(\lambda)$, and hence $\rho'_w(\lambda)$ at each $\tau(865)$. Also given in Table 1 are the corresponding $f(a,b_{bp})$ from Eq. (15). We found earlier (Fig. 3) that $f \ll 1.0$ equates to a good C retrieval for $\tau(865)$ of 0.1 (Section 4.2).

In Fig. 8 we show the ratio of SOA-retrieved C to synthetic C for each of the spectra in Table 1 as a function of S_{CDM}, η and $a^*_{ph}(412)$ described earlier. Results for spectra c1 and c2 are contained in Fig. 8A top and bottom, respectively. Spectra c3 and c4 are in Fig. 8B etc. Variation in $\tau(865)$ is also included in all the graphs. We remind the reader once again that all results are for CBL.

The results clearly show that for each of the four water parameter combinations given (Fig. 8A–D), increasing b_{bp} within each figure (lower row) results in improvement in the C retrieval due to the increase in magnitude of $\rho'_w(\lambda)$. It also completely removes any $\tau(865)$ bias in less turbid waters (Fig. 8A and B) and improves the same bias in high turbidity waters (Fig. 8C and D). This effect is also noticeable by cross comparing figures. The general trend is an improvement in accuracy and decrease in optical depth bias for increasing $\rho'_w(\lambda)$ at blue wavelengths. Interestingly, spectra c5 and c6, and to some extent c7, give the worst results and show largest optical depth dependence. These spectra are characterized by an inverted parabolic spectral shape that is known to the authors to be problematic, i.e., a positive slope between 412 and 490 nm and flat response in the green. Accurate decoupling of $\rho'_A(\lambda)$ and $\rho'_w(\lambda)$ is more difficult for these spectral shapes when the optical depth is large. A repeat of the entire analysis for MAB waters confirms all results in this section. However, the move to these offshore waters is accompanied by a large increase in blue a^*_{ph} and commensurate decrease in blue ρ_w. In the analysis presented above, this is analogous to decreasing b_{bp}. Therefore, a slightly larger $b_{bp}(443)$ is required for the same accuracy.

4.4.4. Performance of SOA with SeaWiFS

We conclude the SOA performance investigation with an illustration of the effect of bio-optical model error using real input data from SeaWiFS. The purpose is to illustrate the relationship between model sensitivity and bio-optical error in a working situation. Calibrated radiance measurements were taken from the SeaWiFS sensor for 26 June 1999 at a pixel centered at 37.50N, 76.08W. This location lies approximately at the center of CBL. A measured C of 4.99 mg m^{-3} (±0.87) was obtained from *in situ* HPLC data at the same location and within 1 h of the satellite scene. The error range corresponds to the standard deviation of this and six additional boat measurements undertaken within 2 h either side of the satellite scan and within a 5 km distance of the given pixel (source: SeaWiFS Bio-optical Algorithm Mini-Workshop data set (O'Reilly et al., 1998)).

SOA retrieves C, $a_{CDM}(443)$, $b_{bp}(443)$, $\tau(865)$ and Junge ν of 5.00 mg m^{-3}, 0.490 m^{-1}, 0.026 m^{-1}, 0.043 and 2.47, respectively. The SOA uses CBL bio-optical coefficients and the near-perfect match up between SOA and *in situ* C was purposely chosen to study the influence of bio-optical model error.

Fig. 9 shows the resulting trends at the same location for C, $a_{CDM}(443)$ and ν (see legend) given introduced SOA error in abscissa S_{CDM}, η, and $a^*_{ph}(412)$ (3 graphs, t–b). The ordinate axis is the retrieved SOA ratio of either C, $a_{CDM}(443)$ or ν to its respective SOA value. There is striking similarity between the C trend in each of the three C curves in Fig. 9 and the three corresponding curves in Fig. 5A, fourth row (l–r) for C=10.0 mg m^{-3}. That is, the SOA C sensitivity as a function of bio-optical error is almost the same when we compared input using synthetic spectra (at C, $a_{CDM}(443)$, $b_{bp}(443)$, $\tau(865)$ of 10.0 mg m^{-3}, 0.5 m^{-1}, 0.03 m^{-1} and 0.1) and real spectra (at 5.00 mg m^{-3}, 0.490 mg m^{-3}, 0.026 m^{-1}, 0.043, respectively). The agreement here indicates that the synthetic analysis in the previous sections is realistic.

In detail, for this station a ±20% error in S_{CDM} results in absolute error of approximately 30% and 20% for C and $a_{CDM}(443)$ respectively. The resulting error in ν is 2–4%. A 20% error in η produces a 5%, 9% and 0.7% error in C, $a_{CDM}(443)$ and ν. Finally, a 20% decrease in $a^*_{ph}(412)$ produces respective error of 12%, 4% and 0.4%. Therefore 20% error in S_{CDM} is most consequential in CBL, and η influences $a_{CDM}(443)$ more than C. Quantity ν is relatively unaffected by η or $a^*_{ph}(412)$.

5. Summary and concluding remarks

In this paper, we have described in detail the implementation of the SOA algorithm for Case 2 waters. The main modification of the SOA for application to Case 2 waters is an iterative scheme for accommodating situations with non-negligible water reflectance in the NIR. Due to the semi-analytic nature of the bio-optical model (GSM), it is a requirement that the three spectral parameters a^*_{ph}, S and η be known *a priori* if the SOA is to be relied upon for $C-a_{CDM}(443)$ retrievals. It is expected that values of these parameters will be site specific and therefore will need to be developed (from *in situ* observations) by the user for application of the algorithm to a specific region.

As mentioned in the introduction, this algorithm will be incorporated into the SeaDAS software package, as an optional processing switch of the Multi-Sensor Level-1 to Level-2 code. This will give the research community the opportunity to utilize and evaluate the approach for other locations and remote sensors. To provide potential users with an understanding of the accuracy and limitations of the algorithm, we generated a synthetic data set to test the performance of the SOA with both correct and incorrect bio-optical model coefficients. Using this data set, we developed two functions, $f(a, b_{bp})$ and $f(a)$, the values of which allow prediction regarding the possible success or failure of the retrieval of C and $a_{CDM}(443)$, respectively: $f(a, b_{bp}) \ll 1$ and $f(a) \sim 1$ for high-quality retrievals. We then showed that C-failure of the algorithm (error in the retrieved C>30%) usually occurs when the water reflectance in the blue becomes ~0.001–0.002 or less, i.e., for "dark waters." For such waters, the SOA will simply not provide useful retrievals. Quantities $a_{CDM}(443)$ and b_{bp} must be correlated in the sense that if $a_{CDM}(443)$ is high b_{bp} must be high (to prevent "dark water"). In practice, it can be argued that high CDM is generally associated with high b_{bp}, as it most often occurs in locations of river outflow and/or sediment resuspension. However low $a_{CDM}(443)$ does not require low b_{bp} as shown in the results. C and b_{bp} will in general be correlated because phytoplankton and their detritus will contribute to b_{bp}; however, if b_{bp} is too low the water could be too "dark" for algorithm success. When there is a positive correlation between $a_{CDM}(443)$ and b_{bp}, we showed that with a ±10% error in S_{CDM} reasonable retrievals of C are usually obtained for $C \geq 0.5$ mg m^{-3} and $a_{CDM}(443) \leq 0.1$ m^{-1} in waters with CBL bio-optics, and for $C \geq 0.1$ mg m^{-3} and $a_{CDM}(443) \leq 0.5$ m^{-1} in waters with MAB bio-optics. Similarly, a ±10% variation in η does not

disrupt good retrievals when $C \geq 0.5$ mg m^{-3} for most $a_{CDM}(443) - b_{bp}$ combinations (showing positive correlations). For $a_{CDM}(443) \geq 0.1$ m^{-1}, the error in the retrieved $a_{CDM}(443)$ will usually be less than 20% as long as C is not too large.

Simulations of the influence of aerosol optical depth suggest that some bias may exist at very low $b_{bp}(443) > 0.005$ m^{-1} and/or under conditions of high aerosol optical depth (≥0.2 at 865 nm). This is most severe in waters with $\rho_w(\lambda)$ spectra characterized by an inverted parabolic shape with limited structure at green wavelengths.

Application of the SOA to actual SeaWiFS data in the CBL (for which surface measurements were available) showed that 20% errors in the bio-optical model parameters still enabled retrieval of C and $a_{CDM}(443)$ with an error of less than 30% and 20%, respectively.

Given realistic coefficients of the bio-optical model, the main weakness of the algorithm is the highly simplified aerosol model. Unfortunately, because of the limited number of spectral bands available, and the desirability of being able to deal (at least approximately) with absorbing aerosols, representation of the aerosol

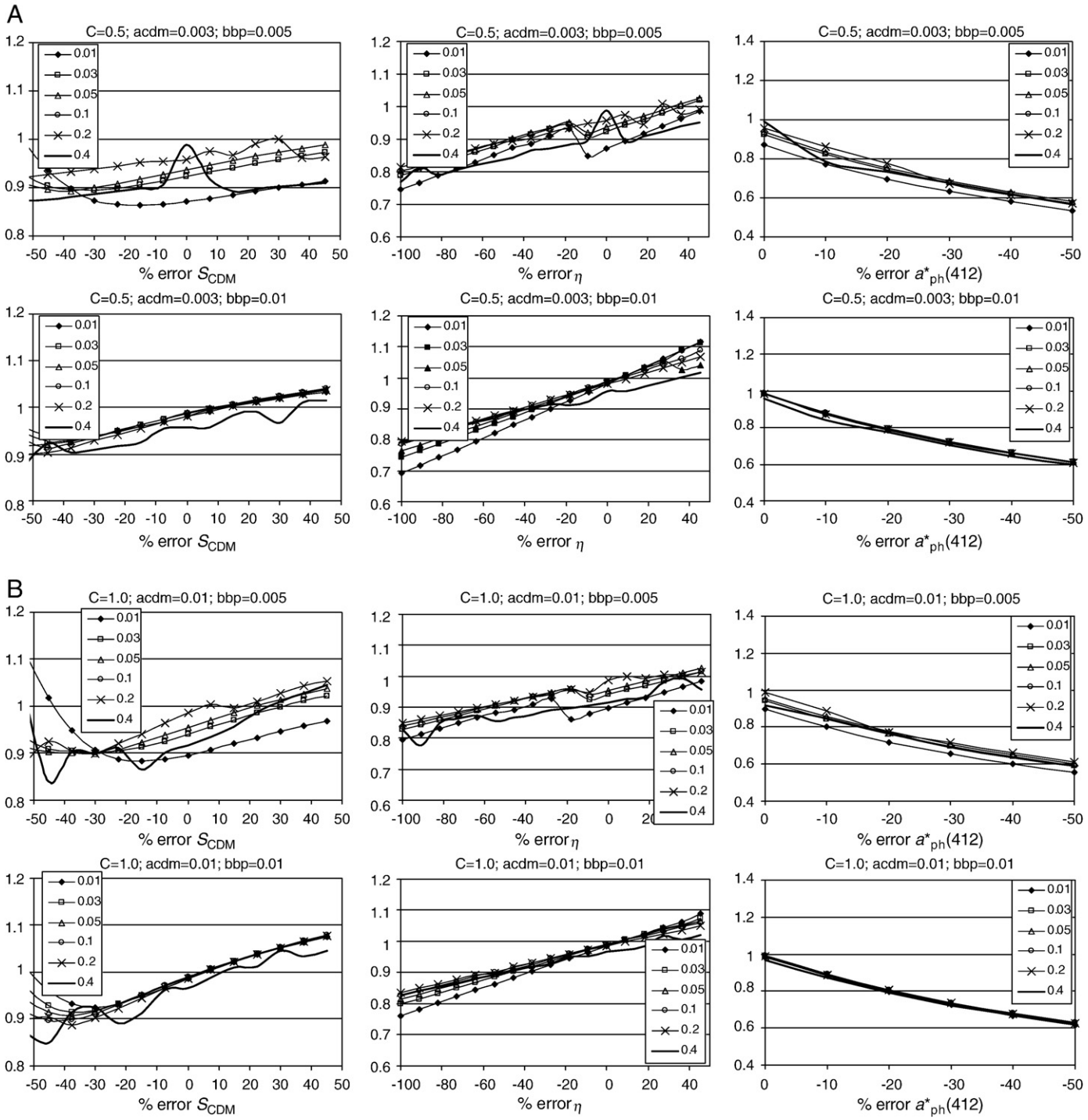

Fig. 8. (A) SOA retrieved C versus synthetic C (y-axis) and its sensitivity to GSM bio-optical coefficients S_{CDM}, η and $a^*_{ph}(412)$ (x-axis, l–r respectively). Results correspond to CBL synthetic ρ_w spectra c1 (top) and c2 (bottom) presented earlier in Table 1 and Fig. 6. Results are shown for all $\tau(865)$ used in this study. B) Same as (A), but for synthetic ρ_w spectra c3 and c4. C) Same as (A), but for synthetic ρ_w spectra c5 and c6. D) Same as (A), but for synthetic ρ_w spectra c7 and c8.

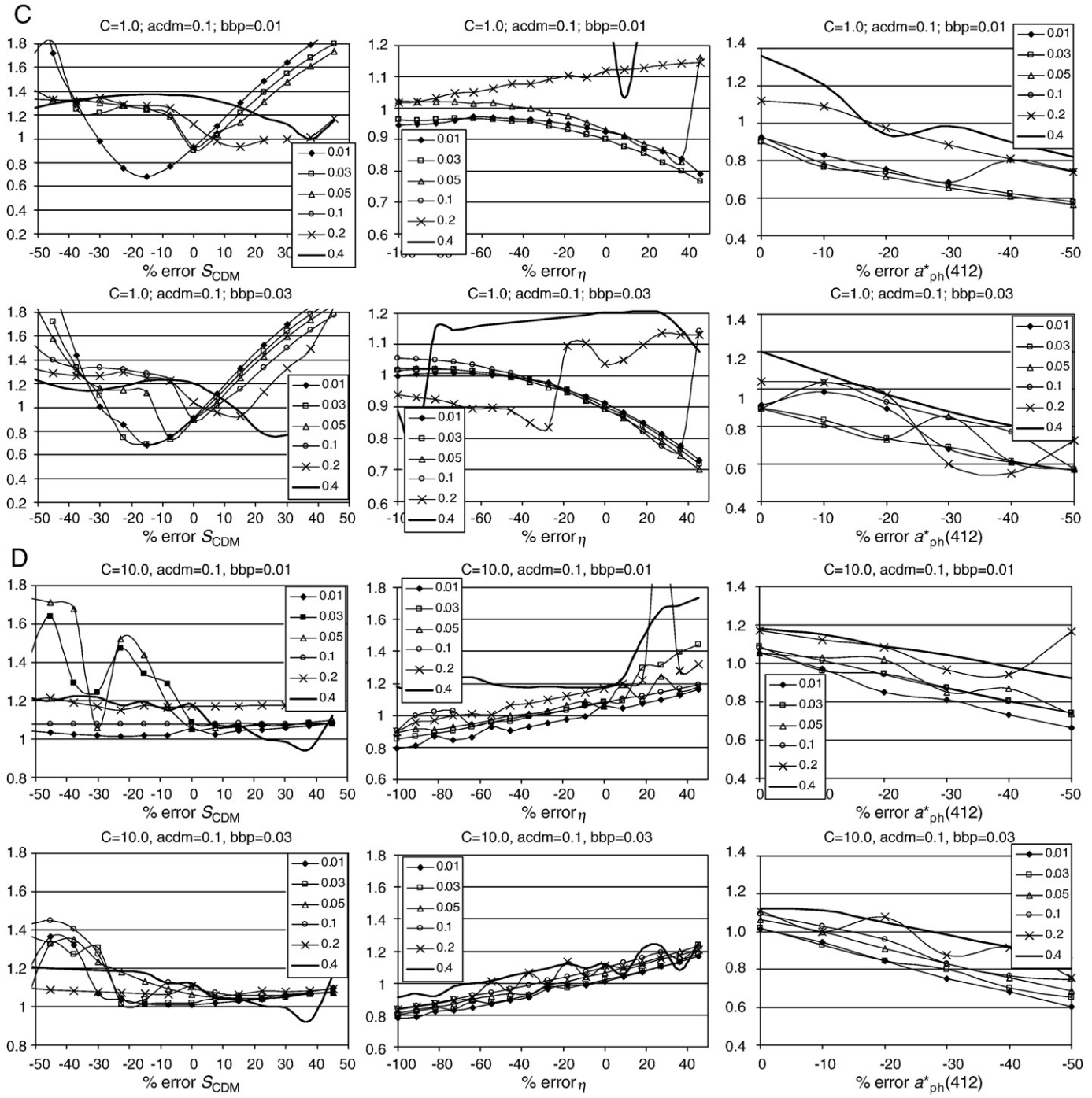

Fig. 8 (*continued*).

size distribution with a single parameter was a necessity. Realistic size distributions would require three to four (or more) parameters.

Acknowledgements

This work was prepared by University of Miami under contracts #NNG04HZ21C and NNX08AH93A from NASA and award #NA17RJ1226 from NOAA/NESDIS, U.S. Department of Commerce. The statements, findings, conclusions and recommendations are those of the authors and do not necessarily reflect the views of NASA, NOAA/NESDIS or the U.S. Department of Commerce.

Appendix. Interpolation of aerosol properties in ν-space

[Estimation of $t^*(\mathrm{NIR},m_r,m_i)$]

We define *candidate* $\nu^{test}(m_r,m_i)$ between 2.0 and 5.0, $\tau^{test}(865,m_r,m_i)$ between 0 and 1.2, and a discrete grid for ν in increments of 0.5 as in the aerosol LUTs (Section 2.2). Quadratic interpolation is then used to derive the extinction coefficient $k(\mathrm{NIR},m_r,m_i,\nu^{test})$ and the NIR diffuse transmittance coefficients $A(\mathrm{NIR},\theta,m_r,m_i,\nu^{test})$ and $B(\mathrm{NIR},\theta,m_r,m_i,\nu^{test})$ from the LUT-gridded ν to the *candidate* ν^{test}. (Note: k is the extinction coefficient of an arbitrary number of particles. It is used solely to provide the wavelength dependence of the optical depth for each model.) For this

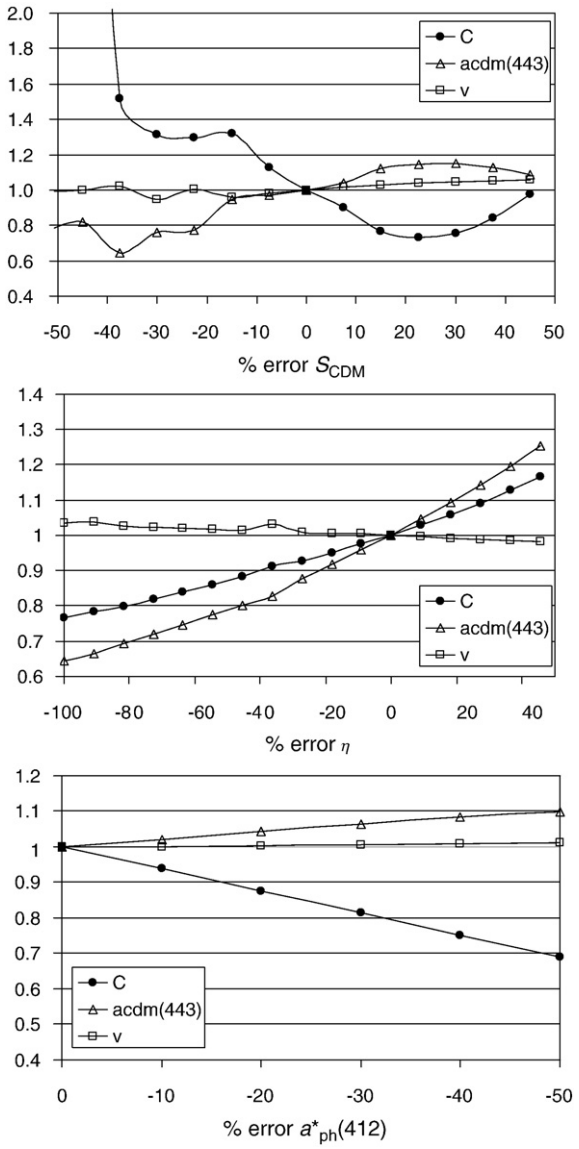

Fig. 9. Ratio of SOA parameter retrieval with bio-optical error versus SOA parameter retrieval with no error (*y*-axis). The three graphs (t–b) correspond to the % error in the three GSM bio-optical coefficients S_{CDM}, η and $a^*_{ph}(412)$ respectively (*x*-axis). Each graph presents three parameters *C*, $a_{CDM}(443)$ and ν. Results are for one pixel in the center of CBL on 26 June 1999 for which SOA and *in situ C* are matched.

purpose, we operate the interpolation across three consecutive ν-grid values that bound *candidate* ν^{test}. If ν^{test} lies outside the ν-grid range, we extend the quadratic shape outside ν-grid, although this rarely occurs. The estimated $\tau^{test}(765,m_r,m_i,\nu^{test})$ in the same ν space is then determined from the *candidate* $\tau^{test}(865,m_r,m_i)$ and interpolated $k(\text{NIR},m_r,m_i,\nu^{test})$ using the equivalence $k(765)/k(865)=\tau(765)/\tau(865)$. (Note that τ^{test} at 765 nm depends not only on m_r and m_i, but also on ν^{test}; hence the addition of ν^{test} to the argument list and its addition to $\tau^{test}(\text{NIR},m_r,m_i,\nu^{test})$ below as well, since "NIR" includes 765 nm.) The diffuse transmittance coefficients along with $\tau^{test}(\text{NIR},m_r,m_i,\nu^{test})$ therefore allow for direct estimation of $t^*(\text{NIR},m_r,m_i,\nu^{test},\tau^{test})$ by Eq. (5).

[Estimation of $\rho_A(\text{NIR},m_r,m_i)$]

An extra step is required for estimation of $\rho'_A(\text{NIR},m_r,m_i,\nu^{test},\tau^{test})$ in ν space. We first take the four coefficients a–$d(\text{NIR},m_r,m_i,G^{grid},\nu^{grid})$ in Eq. (4) and use 2D interpolation in solar/sensor angle and azimuth angle to arrive at updated quantities a–$d(\text{NIR},m_r,m_i,G^{real},\nu^{grid})$. The quantities G^{grid} and G^{real} are the LUT and real sensor geometry, respectively.

Five values of $\tau^{grid}(\text{NIR})$ at 0.05, 0.15, 0.30, 0.60 and 0.80 are then selected. At each τ^{grid}, the geometry-interpolated NIR a–d coefficients are then used to estimate five intermediate values of $\rho'_A(\text{NIR},m_r,m_i,\nu^{grid},\tau^{grid})$ which is then interpolated in ν space by quadratic interpolation as before to give $\rho'_A(\text{NIR},m_r,m_i,\nu^{test},\tau^{grid})$. A fourth order Lagrange polynomial fit is then applied to the set of $\rho'_A(\text{NIR},m_r,m_i,\nu^{test},\tau^{grid})$ values to give estimated quartic coefficients a–$d(\text{NIR},m_r,m_i,G^{real},\nu^{test})$. Hence we have effectively interpolated the original NIR a–d coefficients in geometry and ν space, which along with *candidate* $\tau^{test}(865,m_r,m_i)$ and estimate $\tau^{test}(765,m_r,m_i,\nu^{test})$, allow for estimation of $\rho'_A(\text{NIR},m_r,m_i,\nu^{test},\tau^{test})$ again from Eq. (4).

[Estimation of $t^*(\lambda,m_r,m_i)$, $\rho_A(\lambda,m_r,m_i)$ and $\omega_0(\lambda,m_r,m_i)$]

We now simplify by removing ν^{test} and τ^{test} from the notation. Once optimal functions $\nu(m_r,m_i)$ and $\tau(865,m_r,m_i)$ are established (Eq. (10)), final values of $t^*(\lambda,m_r,m_i)$ and $\rho'_A(\lambda,m_r,m_i)$ are obtained by repeated quadratic interpolation in $\nu(m_r,m_i)$ at all wavelengths. The quantity $\omega_0(\lambda,m_r,m_i)$ from the LUTs is also interpolated in ν space. Note that this procedure uses the same flow as above and therefore computes intermediate quantities $k(\lambda,m_r,m_i,\nu^{test})$, $A(\lambda,\theta,m_r,m_i,\nu^{test})$, $B(\lambda,\theta,m_r,m_i,\nu^{test})$, a–$d(\lambda,m_r,m_i,G^{real},\nu^{test})$ and $\tau^{test}(\lambda,m_r,m_i,\nu^{test})$, i.e., we have found optimal values for all atmospheric parameters at all 12 discrete combinations of m_r, m_i in Section 2.2.

References

Bailey, S. W., & Werdell, P. J. (2006). A multi-sensor approach for the on-orbit validation of ocean color satellite data products. *Remote Sensing Environment*, *102*, 12–23.

Byrd, R. H., Lu, P., & Nocedal, J. (1995). A limited memory algorithm for bound constrained optimization. *SIAM Journal on Scientific and Statistical Computing*, *16*(5), 1190–1208.

Chomko, R. M., Gordon, H. R., Maritorena, S., & Siegel, D. A. (2003). Simultaneous retrieval of oceanic and atmospheric parameters for ocean color imagery by spectral optimization: A validation. *Remote Sensing Environment*, *84*, 208–220.

Chomko, R. M., & Gordon, H. R. (1998). Atmospheric correction of ocean color imagery: Use of the Junge power-law aerosol size distribution with variable refractive index to handle aerosol absorption. *Applied Optics*, *37*, 5560–5572.

Chomko, R. M., & Gordon, H. R. (2001). Atmospheric correction of ocean color imagery: Test of the spectral optimization algorithm with the Sea-viewing Wide Field-of-View Sensor. *Applied Optics*, *40*, 2973–2984.

Ding, K., & Gordon, H. R. (1995). Analysis of the influence of O_2 A-band absorption on atmospheric correction of ocean-color imagery. *Applied Optics*, *34*, 2068–2080.

Franz, B. A., Bailey, S. W., Eplee, R. E., Jr., Feldman, G. C., Kwiatkowska, E., McClain, C., et al. (2005). continuity of ocean color measurements from SeaWiFS to MODIS. *Proceedings of SPIE*, *5882*, 304–316.

Gallegos, C.L., Smithsonian Environmental Research Center, Edge water, MD 20771, USA, personal communication (2006).

Garver, S., & Siegel, D. (1997). Inherent optical property inversion of ocean color spectra and its biogeochemical interpretation: 1 time series from the Sargasso Sea. *Journal of Geophysical Research*, *102C*, 18607–18625.

Gordon, H. R. (1995). Remote sensing of ocean color: a methodology for dealing with broad spectral bands and significant out-of-band response. *Applied Optics*, *34*, 8363–8374.

Gordon, H. R. (1997). Atmospheric correction of ocean color imagery in the Earth observing system era. *Journal of Geophysical Research, D*, *102*, 17,081–17,106.

Gordon, H. R., Clark, D. K., Mueller, J. L., & Hovis, W. A. (1980). Phytoplankton pigments derived from the Nimbus-7 CZCS: Initial comparisons with surface measurements. *Science*, *210*, 63–66.

Gordon, H. R., Brown, O. B., Evans, R. H., Brown, J. W., Smith, R. C., Baker, K. S., et al. (1988). A semi-analytic radiance model of ocean color. *Journal of Geophysical Research, D*, *93*, 10,909–10,924.

Gordon, H. R., & Morel, A. Y. (1983). *Remote assessment of ocean color for interpretation of satellite visible imagery: A review.* New York: Springer-Verlag.

Gordon, H. R., & Wang, M. (1994). Retrieval of water-leaving radiance and aerosol optical thickness over the oceans with SeaWiFS: A preliminary algorithm. *Applied Optics*, *33*, 443–452.

Gordon, H. R., Du, T., & Zhang, T. (1997). Remote sensing ocean color and aerosol properties: Resolving the issue of aerosol absorption. *Applied Optics*, *36*, 8670–8684.

Hooker, S. B., Esaias, W. E., Feldman, G. C., Gregg, W. W., & McClain, C. R. (1992). SeaWiFS Technical Report Series: An Overview of SeaWiFS and Ocean Color. *NASA Tech. Memo 104566 (NASA, Greenbelt, Md., 1992), Vol. 1.*

Hovis, W. A., Clark, D. K., Anderson, F., Austin, R. W., Wilson, W. H., Baker, E. T., et al. (1980). Nimbus 7 coastal zone color scanner: System description and initial imagery. *Science*, *210*, 60–63.

Kaufman, Y. J., Tanre, D., Gordon, H. R., Nakajima, T., Lenoble, J., Frouin, R., et al. (1997). Passive remote sensing of tropospheric aerosol and atmospheric correction for the aerosol effect. *Journal of Geophysical Research*, *102D*, 16815–16830.

Kuchinke, C. P., Gordon, H. R., Harding, L. W., Jr., & Voss, K. J. (2009). Spectral optimization for constituent retrieval in Case 2 waters II: Validation study in the Chesapeake Bay. *Remote Sensing of Environment*, *113*, 610–621. doi:10.1016/j.rse.2008.11.002.

Magnuson, A., Harding, L. W., Jr., Mallonee, M. E., & Adolf, J. E. (2004). Bio-optical model for Chesapeake Bay and the Middle Atlantic Bight. *Estuarine Coastal and Shelf Science*, *61*, 403–424.

Maritorena, S., Siegel, D. A., & Peterson, A. R. (2002). Optimization of semi-analytical ocean color model for global scale applications. *Applied Optics*, *41*, 2705–2714.

Morel, A. (1974). Optical properties of pure water and pure sea water. In N. G. Jerlov, & E. S. Nielson (Eds.), *Optical aspects of oceanography* (pp. 1–24). San Diego, Calif.: Academic.

O'Reilly, J. E., Maritorena, S., Mitchell, B. G., Siegel, D. A., Carder, K. L., Garver, S. A., et al. (1998). Ocean color chlorophyll algorithms for SeaWiFS. *Journal of Geophysical Research*, *103*, 24,937–24,953.

Pope, R. M., & Fry, E. S. (1997). Absorption spectrum (380–700 nm) of pure water. 2. Integrating cavity measurements. *Applied Optics*, *36*, 8710–8723.

Salomonson, V. V., Barnes, W. L., Maymon, P. W., Montgomery, H. E., & Ostrow, H. (1989). MODIS: Advanced facility instrument for studies of the earth as a system. *IEEE Geoscience and Remote Sensing*, *27*, 145–152.

Shettle, E. P., & Fenn, R. W. (1979). Models for the aerosols of the lower atmosphere and the effects of humidity variations on their optical properties. *Rep. AFGL-TR 79-0214, U.S. Air Force Geophysics Laboratory, Hanscom Air Force Base., Mass*.

Siegel, D. A., Wang, M., Maritorena, S., & Robinson, W. (2000). Atmospheric correction of satellite ocean color imagery: The black pixel assumption. *Applied Optics*, *39*(21), 3582–3591.

Tzortziou, M., Herman, J. R., Gallegos, C. L., Neale, P. J., Subramaniam, A., Harding, L. W., Jr., et al. (2006). Bio-optics of the Chesapeake Bay from measurements and radiative transfer closure, Estuarine. *Coastal and Shelf Science*, *68*, 348–362.

Yang, H., & Gordon, H. R. (1997). Remote sensing of ocean color: Assessment of the water-leaving radiance bidirectional effects on the atmospheric diffuse transmittance. *Applied Optics*, *36*, 7887–7897.

Zhu, C., Byrd, R. H., & Nocedal, J. (1997). L-BFGS-B: Algorithm 778: L-BFGS-B, FORTRAN routines for large scale bound constrained optimization. *ACM Transactions on Mathematical Software*, *23*(4), 550–560.